ORIGINAL PAPER

Deformation of salt structures by ice-sheet loading: insights into the controlling parameters from numerical modelling

Jörg Lang[1] · Andrea Hampel[2]

Abstract

Subsurface salt flow is driven by differential loading, which is typically caused by tectonics or sedimentation. During glaciations, the weight of an ice sheet represents another source of differential loading. In salt-bearing basins affected by Pleistocene glaciations, such as the Central European Basin System, ice loading has been postulated as a trigger of young deformation at salt structures. Here, we present finite-element simulations (ABAQUS) with models based on a simplified 50-km long and 10-km-deep two-dimensional geological cross-section of a salt diapir subject to the load of a 300-m-thick ice sheet. The focus of our study is to evaluate the sensitivity of the model to material parameters, including linear and non-linear viscosity of the salt rocks and different elasticities. A spatially and temporarily variable pressure was applied to simulate ice loading. An ice advance towards the diapir causes lateral salt flow into the diapir and diapiric rise. Complete ice coverage leads to downward displacement of the diapir. After unloading, displacements are largely restored. The modelled displacements do not exceed few metres and are always larger in models with linear viscosity than in those with non-linear viscosity. Considering the low stresses caused by ice-sheet loading and the long time-scale, the application of linear viscosity seems appropriate. The elastic parameters also have a strong impact, with lower Young's moduli leading to larger deformation. The impact of both the viscosity and the elasticity highlights the importance of a careful parameter choice in numerical modelling, especially when aiming to replicate any real-world observations.

Keywords Finite-element modelling (ABAQUS) · Salt structures · Salt mechanics · Glaciation · Ice-sheet loading

Introduction

Salt structures, which comprise a variety of salt rocks, are a common feature in sedimentary basins worldwide (e.g., Jackson and Talbot 1986; Jackson et al. 1994; Baldschuhn et al. 1996; Warren 2006; Hudec and Jackson 2007; Fossen 2016). Salt rocks are mechanically weak and deform by viscous flow when subject to stress at geological time scales. The physical processes that contribute to subsurface salt flow include linear solution-precipitation creep and non-linear dislocation creep (Van Keken et al. 1993; Urai et al. 2008). Salt flow is triggered by differential loading, which causes salt to flow from areas of higher load to areas of lower

load. Differential loading is typically related to regional tectonic stresses, gravitational loading by sedimentation or erosion, or tilting of the salt-bearing basin (Jackson and Talbot 1986; Hudec and Jackson 2007). Classic examples of gravitational differential loading by sedimentation are the filling of supra-salt mini-basins (e.g., Waldron and Rygel 2005; Brandes et al. 2012) or the progradation of sediment wedges above a salt layer (e.g., Wu et al. 1990; Vendeville 2005). Salt flow may be induced by small differential loads and does not require the overlying deposits to be denser than the salt (Jackson and Talbot 1986; Cohen and Hardy 1996; Gemmer et al. 2004, 2005; Rowan 2019). The salt-flow rate, the efficiency of salt expulsion from the source layer and the resulting geometries depend primarily on the salt viscosity, the thickness of the source layer and the rate of progradation of the overlying sedimentary systems (e.g., Cohen and Hardy 1996; Gemmer et al. 2004, 2005; Vendeville 2005; Albertz and Ings 2012).

The weight of an ice sheet during a large-scale glaciation can be another source of gravitational differential loading

✉ Jörg Lang
  Joerg.Lang@bgr.de

1 Bundesanstalt für Geowissenschaften und Rohstoffe (BGR), Stilleweg 2, 30655 Hannover, Germany

2 Institut für Geologie, Leibniz Universität Hannover, Callinstraße 30, 30167 Hannover, Germany

that may trigger subsurface salt flow (Liszkowski 1993; Sirocko et al. 2008). Conceptual models suggest that salt rise and uplift above a salt structure will be amplified in ice-marginal settings, where the load of the ice sheet is applied onto the salt source layer (Fig. 1a). In contrast, the rise of salt structures will be hindered or even reversed to subsidence if an ice sheet transgresses a salt structure (Fig. 1b; Liszkowski 1993; Sirocko et al. 2008). In general, these conceptual models have been confirmed by numerical simulations (Kock et al. 2012; Kock 2013; Lang et al. 2014; Baumann et al. 2022; Zill et al. 2022). Notably, the weight of an ice sheet is sufficient to trigger subsurface salt flow although the load is low and transient compared with loading by tectonic or sedimentary processes (Lang et al. 2014).

The Central European Basin System (CEBS) is a key example of a formerly glaciated salt-bearing basin (Fig. 1c). The infill of the CEBS is characterised by a multitude of salt structures that comprise Permian Zechstein salt and display a variety geometries (Fig. 1c, d; Doornenbal and Stevenson

2010; Warsitzka et al. 2019). Initial salt movement in the CEBS began in the Early Triassic and continued in several phases until the Late Cenozoic (Jaritz 1973; Kockel 2003; Warsitzka et al. 2019). During the Pleistocene, large parts of the CEBS were repeatedly transgressed by major ice sheets. In the German part of the CEBS, for example, every salt structure was at least twice covered by the ice sheets, while salt structures farther to the northeast were covered by ice sheets even more often (Fig. 1c; Ehlers et al. 2011; Lang et al. 2014, 2018; Winsemann et al. 2020). Pleistocene or Holocene salt movements have been inferred for a number of salt structures in this area. However, it remains unresolved if Pleistocene and Holocene salt movements are the continuation of pre-Pleistocene processes controlled by the regional stress field or if ice-sheet loading triggered a reactivation (Sirocko et al. 2008; Al Hseinat et al. 2016; Hardt et al. 2021).

The response of the salt rocks within a salt structure to an external load is controlled by a range of parameters.
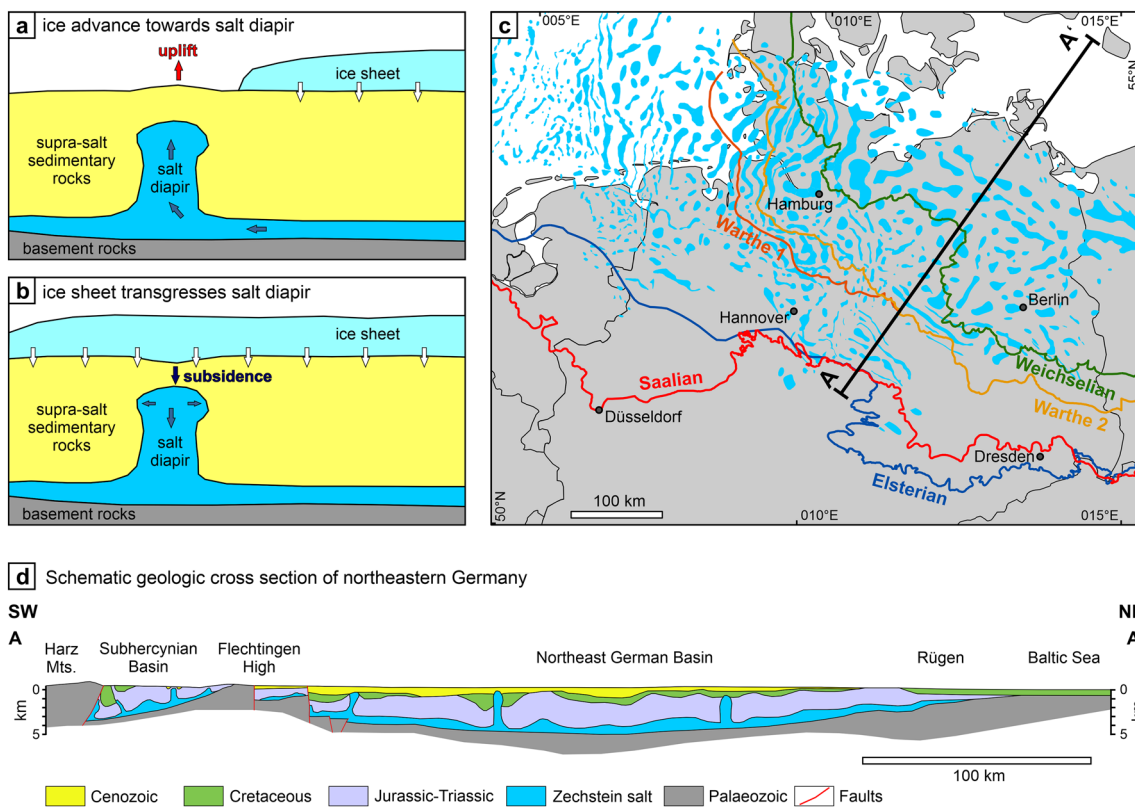

Fig. 1 **a**, **b** Conceptual model of the response of a salt diapir to ice-sheet loading (modified after Lang et al. 2014). **a** An ice advance towards a salt diapir causes lateral salt flow from the salt-source layer into the diapir, leading to the rise of the diapir and uplift. **b** When the ice sheet transgresses the diapir, the diapir is pushed downwards and broadens, leading to subsidence above the diapir. **c** Map of the salt structures (blue) and maximum ice-sheet extents in the German part of the Central European Basin System. Salt structures are from Doornenbal and Stevenson (2010), ice-sheet extents are compiled from Ehlers et al. (2011), Lang et al. (2018) and Winsemann et al. (2020). **d** Schematic geologic cross-section of northeastern Germany, showing the characteristic architecture of the basin fills, including several salt structures (modified after DEKORP-BASIN Research Group 1999). The location of the cross-section is indicated by the black line (A–A') in (**c**)

Important controlling factors include the material properties of the salt and the supra-salt rocks, the size and geometry of the salt structure and the magnitude of the load. Previous studies of the response of salt structures to ice-sheet loading indicate that larger displacements are mainly related to more mobile salt, larger amounts of salt rocks involved, larger loads and longer loading phases (Kock et al. 2012; Kock 2013; Lang et al. 2014; Zill et al. 2022).

The major challenge with respect to a better understanding of the response of salt structures to ice-sheet loading and the modelling of such processes is the multitude of controlling factors. The ice load depends on the ice-sheet thickness, the ice-advance and retreat rates and the duration of ice coverage. However, these factors are highly variable in space and time and are typically poorly constrained for specific locations (e.g., Lambeck et al. 2010; Hughes et al. 2016; Lang et al. 2018). In contrast, the mechanical behaviour of the involved geological materials is generally better constrained. However, different approaches exist to describe the rheologies, resulting in a large number of constitutive equations and material parameters (e.g., Van Keken et al. 1993; Ter Heege et al. 2005; Urai et al. 2008). The description of the involved materials is further complicated by the heterogeneity and complex geometries of real rocks.

The aim of this study is to investigate the controlling factors of the ice load-driven deformation of salt structures. The focus is on the impact of different rheologies of the geological materials on the model results. Parameters such as the viscosity of the salt rocks, the elasticity of the supra-salt rocks and the geometry and internal architecture of the salt structure were systematically varied to determine their respective impact. For the salt rocks, both linear and non-linear viscosities were tested. Furthermore, the elasticity of the salt and non-salt rocks was varied. Salt structures typically display complex internal architectures that comprise evaporitic and non-evaporitic strata. The presence of internal strata with contrasting rheologies may affect the mobility of the entire salt structure. Therefore, salt structures with an internal architecture including layers of very low viscosity (representing potassium salt) or very high viscosity (representing anhydrite), respectively, were modelled to test how the internal architecture and different rheologies affect the results. This study is deliberately intended not to replicate any real-world scenarios although the model setup is inspired by salt diapirs in the CEBS. Instead, the model results will help to evaluate deformation structures and displacements observed at salt structures in nature in the context of ice-sheet loading as a trigger mechanism. The results will also yield important implications for the long-term safety of waste repositories build into salt structures. Such safety assessments need to cover the next 100,000 to 1,000,000 years, making the consideration of the impact of future glaciations necessary. Assessments of the long-term safety of repositories rely heavily on numerical simulations and an appropriate parameter choice, based on natural examples, is of paramount importance. The insights gained from this parameter study can also be applied in more general studies of the evolution of salt structures. Furthermore, the results contribute to a better understanding of recent salt-tectonic deformation observed in formerly glaciated basins.

Mechanical behaviour of rock salt

Salt rocks are mechanically weak and are commonly regarded as behaving like viscous fluids when deforming at geological time scales and strain rates (e.g., Jackson et al. 1994; Hudec and Jackson 2007; Fossen 2016). The viscosity of natural rock salt is affected by the salt mineralogy, temperature, water content and grain size and the viscosity varies over several orders of magnitude (Van Keken et al. 1993; Weijermars et al. 1993; Mukherjee et al. 2010). The strain rates in deforming salt bodies typically range from 2×10^{-16} to 8×10^{-11} s^{-1}, corresponding to salt-flow rates of 1×10^{-2} to 2 mm $\times$ a^{-1} (Jackson & Vendeville 1994; Jackson et al. 1994; Warren 2006). The differential stresses that drive salt-tectonic deformation typically range from 0.5 to 3 MPa with higher differential stresses of up to 5 MPa occurring at shallow depths (Carter et al. 1982; Spiers and Carter 1998; Schléder and Urai 2005, 2007; Li et al. 2012; Henneberg et al. 2018, 2022; Kneuker et al. 2018).

The physical mechanisms responsible for the viscous flow of rock salt are dislocation creep and solution-precipitation creep. During subsurface salt deformation and salt-tectonic processes, both mechanisms contribute to salt flow. The dominant deformation mechanism depends on the stress magnitude, confining pressure, temperature, fluid content and pressure, grain size, impurities and anisotropy (Van Keken et al. 1993; Ter Heege et al. 2005; Warren 2006; Urai et al. 2008; Kneuker et al. 2018).

Dislocation creep is caused by defects in the crystal lattice and the development of subgrains that lead to dislocations. Dislocation creep is a non-linear process, where the strain rate $\dot{\varepsilon}$ is related to the differential stress using a power-law equation (Fig. 2; Carter and Hansen 1983; Van Keken et al. 1993; Hunsche and Hampel 1999; Urai et al. 2008):

$$\dot{\varepsilon} = A * \Delta\sigma^n = A_0 \exp\left(-\frac{Q}{R * T}\right) * \Delta\sigma^n$$

The differential stress $\Delta\sigma$ is defined as $\Delta\sigma = \sigma_1 - \sigma_3$ where σ_1 and σ_3 are the maximum and minimum principal stresses, respectively. The value of the power-law exponent n typically ranges from 1 to 7. The factor A summarises the viscous behaviour of the salt and is defined by a material-dependent parameter A_0, the specific activation energy Q,

Fig. 2 Plot of the differential stress versus strain rate for non-linear dislocation creep, linear solution-precipitation creep and linear viscosity. Data for the plots are compiled from Spiers et al. (1990), Jackson and Vendeville (1994), Hunsche and Hampel (1999) and Li et al. (2012)
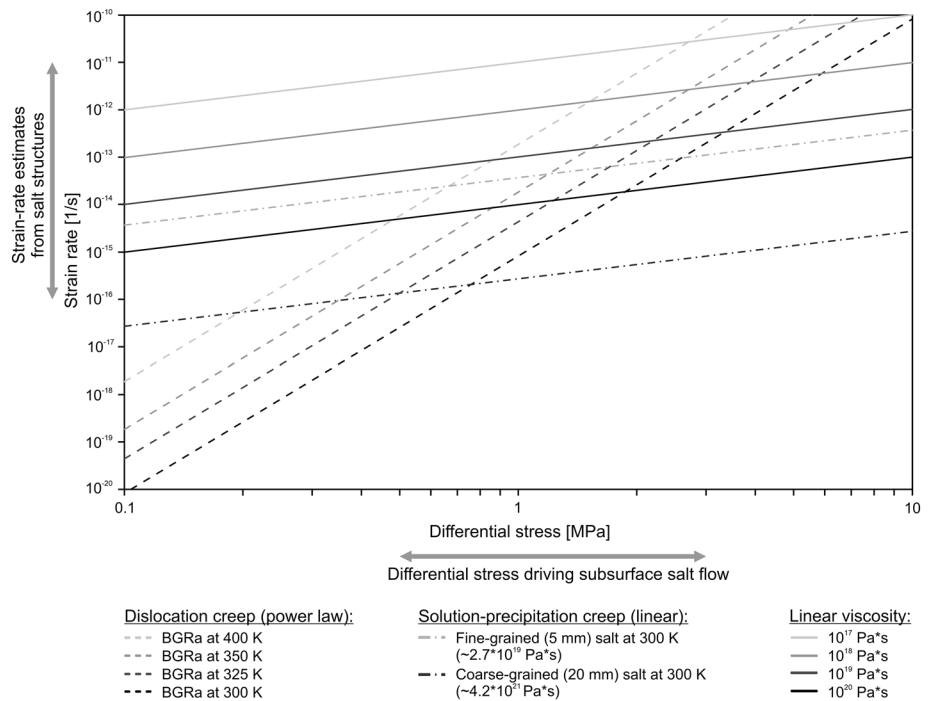
the universal gas constant R (8.314 J mol^{-1} K^{-1}) and the temperature T. The temperature strongly affects the strain rate for power-law creep (Fig. 2). Values of the material parameter A_0 are mostly derived from creep experiments.

Solution-precipitation creep—also called pressure-solution or diffusion creep—is related to sliding along the crystal-grain boundaries and fluid-enhanced dynamic recrystallisation, involving mass transfer at grain boundaries. Dissolution occurs at grain boundaries under high stress, followed by diffusion through the grain-boundary fluid and recrystallisation in areas of lower stress (Carter and Hansen 1983; Spiers et al. 1990; Urai et al. 2008; Li and Urai 2016). For solution-precipitation creep, the strain rate is linearly related to the differential stress (Fig. 2; Spiers et al. 1990; Li and Urai 2016):

$$\dot{\varepsilon} = B * \Delta\sigma = B_0 \exp\left(-\frac{Q}{R*T}\right) * \left(\frac{1}{T*D^3}\right) * \Delta\sigma$$

The factor B summarises the viscosity of the salt, B_0 is a material-dependent parameter and D is the mean grain size. Solution-precipitation creep is strongly grain-size dependant (Fig. 2). Solution-precipitation creep is a fluid-assisted process mostly active in wet rock salt with a brine content of 10–20 ppm (Urai et al. 2008). Values for the material parameter B_0 and the activation energy Q are derived empirically (e.g., Spiers et al. 1990). However, pressure-solution creep is hardly observed in experiments due to the limited time, low water content and high stresses (Li and Urai 2016; Bérest et al. 2019).

In geological models designed to reconstruct or predict the evolution of salt structures at large temporal (10^3 to 10^8 a) and spatial (10^3 to $10^{6\,m}$) scales salt creep is usually simplified to a linear (Newtonian) viscosity (Gemmer et al. 2004, 2005; Albertz and Ings 2012; Nikolinakou et al. 2012, 2014; Rowan et al. 2019; Granado et al. 2021). The constitutive equation for linear viscous materials is

$$\dot{\varepsilon} = \frac{\Delta\sigma}{\eta}$$

The simplification of applying a constant linear viscosity can be justified as linear solution-precipitation creep is considered as the dominant mechanism at the time scales, stress and strain rates relevant for geological processes (Urai et al. 1986, 2008; Weijermars et al. 1993). The linear viscosity η basically summarises all factors that define solution-precipitation creep. Estimates of the viscosity η of rock salt typically range from 10^{16} to 10^{20} Pa s (Van Keken et al. 1993; Weijermars et al. 1993; Mukherjee et al. 2010; Rowan et al. 2019).

Methods

Model set-up

Finite-element simulations of the interaction between salt diapirs and ice sheets were conducted using the commercial software ABAQUS (Version: ABAQUS 2020). The 2D

models were based on a 50 km long and 10 km deep schematic geological cross-section (Figs. 3, 4). The models were meshed using 2D triangular plain-strain elements. The initial edge length of the elements was set to 10 m in the section representing the salt diapir and increased to 50 and 400 m at the sides and the base of the section, respectively. The nodes at the model sides were fixed in horizontal (x) direction and free in vertical (y) direction, while the nodes at the model base were fixed in vertical and horizontal direction.

Tested configurations

A number of model configurations were tested to evaluate the impact of different parameters on the modelling results (Table 1). The tested parameters include the geometry of the geological cross-section, the rheology of the materials, the location of the ice margin and the duration of the different model steps.

Fig. 3 Conceptual sketch of the model set-up. The modelled section comprises viscoelastic salt and elastic basement and supra-salt rocks. The model sides are fixed in x-direction, the model base is fixed in x- and z-directions. Ice-sheet loading is simulated by the loading and unloading of the four surface sections
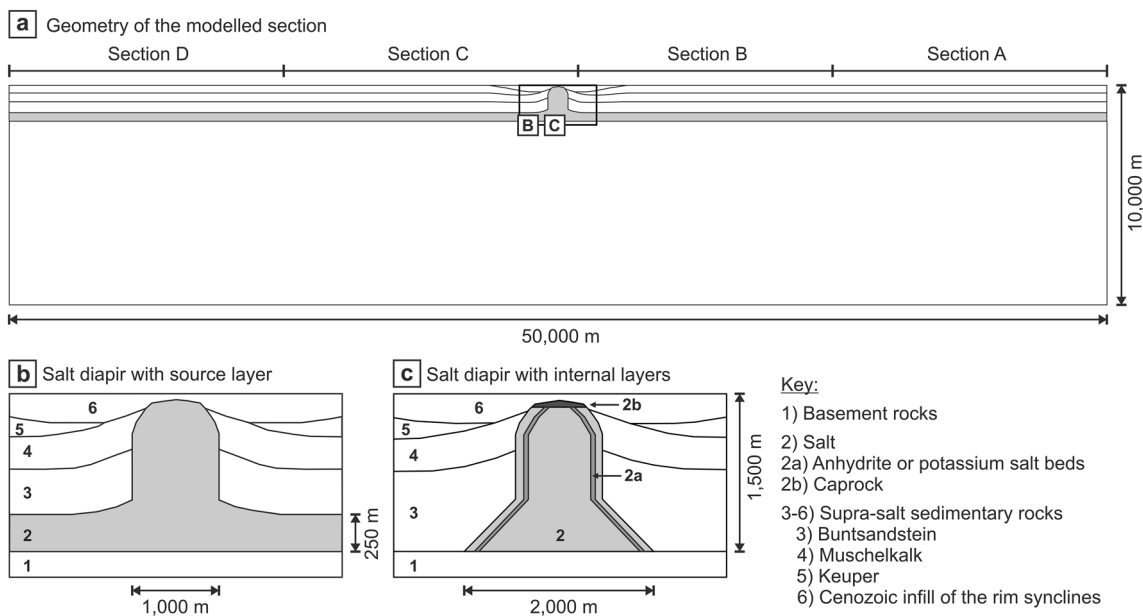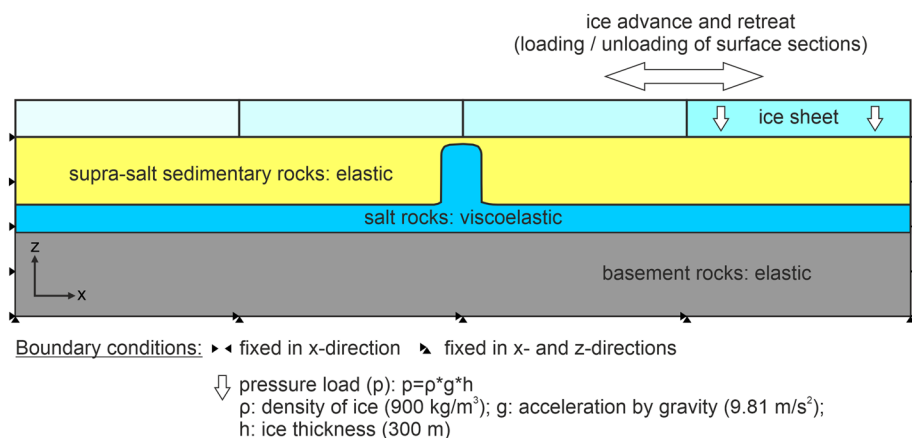
Fig. 4 Geometry of the modelled section. **a** Overview of the modelled section. The section comprises a viscoelastic salt layer and diapir and elastic basement and supra-salt rocks. The model surface is partitioned into four sections that can be loaded and unloaded to simulate the advance and retreat of an ice sheet. **b** Detail of the model geometry with a salt diapir and a 250-m-thick salt-source layer. The salt-source layer extends laterally to the margins of the section. **c** Detail of the model geometry with a salt pinch-out 1000 m from the model centre. The salt diapir includes two internal layers and a caprock layer

Table 1 Tested configurations

Name	Geometry	Viscous behaviour				Elastic behaviour	Ice coverage	Duration of steps				Remarks
		Linear viscosity		Non-linear viscosity				Ice advance	Maximum ice extent	Ice retreat	Ice-free	
		Main salt body	Internal layers	Main salt body	Internal layers							
BM-A8	Simple salt structure with source layer	10^{18} Pa s	–	–	–	Set "RK"	Complete	3×150 a	5000 a	3×150 a	10000 a	–
BM-A8ex	Simple salt structure with source layer	10^{18} Pa s	–	–	–	Set "RK"	Complete	3×150 a	15000 a	3×150 a	20000 a	–
BM-A9	Simple salt structure with source layer	–	–	BRGa at 325 K	–	Set "LA"	Complete	3×150 a	5000 a	3×150 a	10000 a	–
BM-A9ex	Simple salt structure with source layer	–	–	BRGa at 325 K	–	Set "LA"	Complete	3×150 a	15000 a	3×150 a	20000 a	–
BM-A10	Simple salt structure with source layer	–	–	BRGa at 325 K	–	Set "RK"	Complete	3×150 a	5000 a	3×150 a	10000 a	–
BM-A11	Simple salt structure with source layer	10^{18} Pa s	–	–	–	Set "LA"	Complete	3×150 a	5000 a	3×150 a	10000 a	–
BM-A11ex	Simple salt structure with source layer	10^{18} Pa s	–	–	–	Set "LA"	Complete	3×150 a	15000 a	3×150 a	20000 a	–
BM-A12	Simple salt structure with source layer	10^{20} Pa s	–	–	–	Set "LA"	Complete	3×150 a	5000 a	3×150 a	10000 a	–
BM-A12ex	Simple salt structure with source layer	10^{20} Pa s	–	–	–	Set "LA"	Complete	3×150 a	15000 a	3×150 a	20000 a	–
BM-A13	Simple salt structure with source layer	–	–	–	–	Set "LA"	Complete	3×150 a	5000 a	3×150 a	10000 a	No viscosity

Table 1 (continued)

Name	Geometry	Viscous behaviour				Elastic behaviour	Ice coverage	Duration of steps				Remarks
		Linear viscosity		Non-linear viscosity				Ice advance	Maximum ice extent	Ice retreat	Ice-free	
		Main salt body	Internal layers	Main salt body	Internal layers							
BM-A14	Simple salt structure with source layer	–	–	BGRa at 300 K	–	Set "LA"	Complete	3×150 a	5000 a	3×150 a	10000 a	–
BM-A15	Simple salt structure with source layer	–	–	BRGa at 325 K	–	Set "LA"	Complete	3×150 a	5000 a	3×150 a	10000 a	–
BM-A16	Simple salt structure with source layer	–	–	BGRa at 350 K	–	Set "LA"	Complete	3×150 a	5000 a	3×150 a	10000 a	–
BM-A17	Simple salt structure with source layer	–	–	BGRa at 400 K	–	Set "LA"	Complete	3×150 a	5000 a	3×150 a	10000 a	–
BM-A18	Simple salt structure with source layer	10^{19} Pa s	–	–	–	Set "LA"	Complete	3×150 a	5000 a	3×150 a	10000 a	–
BM-A19	Simple salt structure with source layer	–	–	BRGa at 325 K	–	Set "RK"	Complete	3×150 a	5000 a	3×150 a	10000 a	–
BM-A20	Simple salt structure with source layer	–	–	–	–	Set "RK"	Complete	3×150 a	5000 a	3×150 a	10000 a	No viscosity
BM-A21	Simple salt structure with source layer	10^{16} Pa s	–	–	–	Set "LA"	Complete	3×150 a	5000 a	3×150 a	10000 a	–
BM-A22	Simple salt structure with source layer	10^{18} Pa s	–	–	–	Set "LA"	Complete	3×150 a	5000 a	3×150 a	10000 a	Depth to top salt 250 m

Table 1 (continued)

Name	Geometry	Viscous behaviour				Elastic behaviour	Ice coverage	Duration of steps				Remarks
		Linear viscosity		Non-linear viscosity				Ice advance	Maximum ice extent	Ice retreat	Ice-free	
		Main salt body	Internal layers	Main salt body	Internal layers							
BM-A23	Simple salt structure with source layer	10^{18} Pa s	–	–	–	Set "LA"	Complete	3×150 a	5000 a	3×150 a	10000 a	No "Cenozoic rim-syncline fill"
S1_L_La	Salt structure with internal layers and caprock	10^{18} Pa s	10^{18} Pa s	–	–	Set "LA"	Complete	3×150 a	5000 a	3×150 a	10000 a	–
S1_NL_La	Salt structure with internal layers and caprock	–	–	BRGa at 325 K	BRGa at 325 K	Set "LA"	Complete	3×150 a	5000 a	3×150 a	10000 a	–
S1_L_RK	Salt structure with internal layers and caprock	10^{18} Pa s	10^{18} Pa s	–	–	Set "RK"	Complete	3×150 a	5000 a	3×150 a	10000 a	–
S1_NL_RK	Salt structure with internal layers and caprock	–	–	BRGa at 325 K	BRGa at 325 K	Set "RK"	Complete	3×150 a	5000 a	3×150 a	10000 a	–
S1_Hvis_La	Salt structure with internal layers and caprock	10^{20} Pa s	10^{20} Pa s	–	–	Set "LA"	Complete	3×150 a	5000 a	3×150 a	10000 a	–
S1_Lvis_La	Salt structure with internal layers and caprock	10^{16} Pa s	10^{16} Pa s	–	–	Set "LA"	Complete	3×150 a	5000 a	3×150 a	10000 a	–
S2_Anh	Salt structure with internal layers and caprock	10^{18} Pa s	10^{23} Pa s	–	–	Set "LA"	Complete	3×150 a	5000 a	3×150 a	10000 a	–
S2_Kali	Salt structure with internal layers and caprock	10^{18} Pa s	$3.5*10^{13}$ Pa s	–	–	Set "LA"	Complete	3×150 a	5000 a	3×150 a	10000 a	–

Table 1 (continued)

Name	Geometry	Viscous behaviour				Elastic behaviour	Ice coverage	Duration of steps				Remarks
		Linear viscosity		Non-linear viscosity				Ice advance	Maximum ice extent	Ice retreat	Ice-free	
		Main salt body	Internal layers	Main salt body	Internal layers							
BM-H11	Simple salt structure with source layer	–	–	10^{18} Pa s	–	Set "LA"	Partial	150 a	10000 a	150 a	10000 a	–
BM-H12	Simple salt structure with source layer	–	–	BRGa at 325 K	–	Set "LA"	Partial	150 a	10000 a	150 a	10000 a	–
BM-H13	Simple salt structure with source layer	–	–	10^{18} Pa s	–	Set "RK"	Partial	150 a	10000 a	150 a	10000 a	–

Geometry of the modelled section

The internal geometry of the modelled section was modified from Lang et al. (2014). The original section represents a simplified geological cross-section from a salt structure in the Subhercynian Basin at the southern margin of the Central European Basin System (Fig. 1d; Baldschuhn et al. 1996; Brandes et al. 2012). The selected example salt structure actually forms part of a salt wall with a length of ~70 km (Brandes et al. 2012). However, in the modelled cross-section, it appears as a two-dimensional salt diapir. The geological cross-section represents a symmetrical salt diapir, supra-salt rocks, including the infill of symmetrical rim synclines, and basement rocks (Fig. 4). The supra-salt rocks comprise three different stratigraphic units that represent rocks of the Triassic Buntsandstein, Muschelkalk and Keuper Groups and the Cenozoic infill of the rim synclines (Fig. 4; Tables 2, 3). The base of the diapir is 1500 m deep. The top of the diapir has a depth of 50 m. The diapir has a width of 1000 m. The rim synclines are 6 km wide and up to 300 m deep. The basement is a single unit that begins at a depth of 1500 m and extends to the base of the model at a depth of 10000 m (Fig. 4).

The first model series was run using sections with a 250-m-thick salt source layer, which extended laterally from the diapir to the margins of the section (Fig. 4a, b). Internally, the salt structure in the first model series was homogeneous. In the second model series, the salt layer pinches-out 1000 m from the centre of the section (Fig. 4c). The uppermost ~50 m of the diapir was defined as caprock. Internally, two steeply dipping, up to 25-m-thick layers were included. These layers could be attributed different properties to represent either beds of potassium salt or anhydrite (Table 4).

Rheology of the model materials

The material parameters were defined to resemble the rheologies of natural sedimentary rocks. The supra-salt and basement rocks were treated as elastic, while the salt rocks were treated as viscoelastic.

The elastic behaviour of the different materials was defined by their Young's Moduli (E) and Poisson's ratios (ν). Two different sets of these parameters were tested (Table 2). Parameter set "LA" was taken from previous models of Lang et al. (2014). Parameter set "RK" was based on parameters that have been applied numerical simulations in the context of the long-term safety of radioactive waste repositories (e.g., Liu et al. 2017; Bertrams et al. 2020).

To simulate the viscous behaviour of salt rocks both linear and non-linear creep was implemented. For non-linear viscosity, the so-called "BGRa" creep law was applied, which describes the temperature- and stress-dependent steady-state creep of salt rocks (Hunsche and Schulze 1994; Hunsche

and Hampel 1999). The BGRa creep law was developed to predict the long-term temporal and spatial development of stress and deformation in underground workings (Bräuer et al. 2011). The BGRa creep law describes power-law creep with an exponent of $n = 5$, a pre-exponential material parameter $A_0 = 2.08*10^{-6}$ s^{-1} and an activation energy $Q = 54000$ J mol^{-1} (Hunsche and Schulze 1994; Hunsche and Hampel 1999). To account for the temperature dependency, temperatures of 300, 325, 350 and 400 K were tested. A temperature of 325 K was chosen as representing the reference temperature. The temperature gradient in the subsurface and temperature changes during a glacial cycle were not considered. It should be noted that the BGRa creep law was defined for specific, homogeneous rock-salt lithologies. For other salt-rock lithologies, the equation needs to be modified by an additional pre-exponential factor, which typically ranges from 1/64 to 16 and defines the so-called creeping class (Hunsche and Hampel 1999; Hunsche et al. 2003; Kock et al. 2012; Liu et al. 2017).

For linear viscosity, viscosities ranging from 10^{16} to 10^{20} Pa*s were tested (Tables 1, 4). A viscosity of 10^{18} Pa*s was chosen as representing the reference viscosity, which is in line with previous numerical models of salt tectonics (e.g., Gemmer et al. 2004, 2005; Albertz and Ings 2012; Nikolinakou et al. 2012; Granado et al. 2021). In models that included internal layers within the salt structure, linear viscosities of 10^{13} and 10^{23} Pa*s were used for potassium salt and anhydrite, respectively.

Table 2 Material parameter set "LA" for supra-salt sedimentary rocks and basement rocks

Parameter set	Model unit	Lithostratigraphic unit	Lithologies	Density ρ (kg/m^3)	Elastic modulus E (MPa)	Poisson ratio ν_P (–)	Source
LA	Cenozoic rim syncline	Cenozoic	Poorly consolidated siliciclastics	2000	5000	0.25	Lang et al. (2014)
LA	Supra-salt sedimentary cover	Keuper (Triassic)	Marlstone and sandstone	2500	40000	0.25	Lang et al. (2014)
LA	Supra-salt sedimentary cover	Muschelkalk (Triassic)	Limestone and marlstone	2600	50000	0.25	Lang et al. (2014)
LA	Supra-salt sedimentary cover	Buntsandstein (Triassic)	Mudstone and sandstone	2600	50000	0.25	Lang et al. (2014)
LA	Caprock	Caprock (Perminan)	Caprock	2300	500	0.25	Liu et al. (2017); Bertrams et al. (2020)
LA	Basement	Palaeozoic	Sedimentary rocks	2700	60000	0.25	Lang et al. (2014)

Table 3 Material parameter set "RK" for supra-salt sedimentary rocks and basement rocks

Parameter set	Model unit	Lithostratigraphic unit	Lithologies	Density ρ (kg/m^3)	Elastic modulus E (MPa)	Poisson ratio ν_P (–)	Source
RK	Cenozoic rim syncline	Cenozoic	Poorly consolidated siliciclastics	2100	500	0.33	Liu et al. (2017); Bertrams et al. (2020)
RK	Supra-salt sedimentary cover	Keuper (Triassic)	Marlstone and sandstone	2600	12000	0.27	Liu et al. (2017); Bertrams et al. (2020)
RK	Supra-salt sedimentary cover	Buntsandstein-Muschelkalk (Triassic)	Limestone, marlstone, mudstone and sandstone	2500	15000	0.27	Liu et al. (2017); Bertrams et al. (2020)
RK	Caprock	Caprock (Permian)	Caprock	2300	500	0.27	Liu et al. (2017); Bertrams et al. (2020)
RK	Basement	Palaeozoic	Sedimentary rocks	2500	17000	0.27	Liu et al. (2017); Bertrams et al. (2020)

Ice-sheet loading

Loading by the weight of an ice sheet was simulated as a pressure load that was applied at the surface of the model. The magnitude of the pressure load was ~2.65 MPa, corresponding to the weight of a 300-m-thick ice sheet. Such a thickness can be expected within a distance of 5–50 km from the margin of an ice sheet (Benn and Hutton 2010; Beaud et al. 2016). The surface profile of the ice sheet was not considered for simplicity and to avoid additional horizontal stresses in the upper units of the model (cf., Andersen et al. 2005). To simulate the advance and retreat of an ice sheet across the geological section, the surface of the model was subdivided into four segments that could be independently loaded and unloaded (Fig. 4a). During the ice-sheet advance, the surface segments were sequentially loaded, beginning at the right-hand side of the model. Complete ice coverage was represented by a step where all segments of the surface were loaded. During ice-sheet retreat the segments were sequentially unloaded, beginning at the left-hand side of the model. Loading and unloading of the individual surface segments was instantaneously. In the last step of each run no load was applied, representing post-glacial conditions.

Two different configurations of the ice-sheet extent were tested. In models with complete ice coverage, all four surface sections were loaded during the step representing the maximum ice-sheet extent (Fig. 4a). In models with partial ice coverage, only the two surface sections at the right-hand side of the model (sections A and B) were loaded during the step of the maximum ice-sheet extent. In this configuration, the ice margin was located next to the diapir, but the ice sheet did not transgress the diapir (Fig. 4a).

The duration of the modelling steps that represented the ice advance and retreat was 150 a for each step. As the surface sections are 12.5 km long, this corresponds to advance and retreat rates of 75 m*a^{-1}. The duration of the glacial maximum step was set to 5000 or 15000 a, respectively. The durations and advance/retreat rates are within the range of those estimated for Pleistocene continental ice sheets (e.g., Ehlers 1990; Lüthgens et al. 2011; Hughes et al. 2016; Lang et al. 2018). The load-free post-glacial step had a duration of 10000 or 20000 a, respectively. After these durations, rates of displacement observed in the models became very low.

Results

The models show the deformation of the salt diapir and overlying strata during the advance and retreat of an ice sheet (Figs. 5, 6). Deformation in the sub-salt basement rocks is restricted to some vertical compression by the weight of the ice sheet (Fig. 5). The initial advance of the ice sheet commonly leads to some uplift at the top of the diapir (Fig. 5a). Uplift is caused by lateral salt flow from the source layer into the diapir due to the applied differential load by partial loading of the model surface (steps GA-1 and GA-2; Fig. 5a, c). Some uplift may also be related to the increased stress in the supra-salt rocks, potentially causing horizontal extension that exerts additional stress on the salt diapir. The uplift increases for longer periods of partial loading and lower viscosity salt. The observed maximum uplift was ~1.4 m. In models with high-viscosity salt, the initial uplift due to salt flow is very small and exceeded by downwards displacement of the whole model surface due to the elasticity of the material (Fig. 7a).

When the salt diapir is transgressed by the ice sheet, the top of the diapir is displaced downwards, leading to subsidence at the surface above the diapir (steps GA-3 and Gmax; Fig. 6b, c). The downward displacement is accompanied by some broadening of the diapir (Fig. 6c). Depending on the chosen parameters, the downwards displacement may

Table 4 Material parameters for viscous salt rocks

Model unit	Lithostratigraphic unit	Lithology	Density ρ (kg/m^3)	Elastic modulus E (MPa)	Poisson ratio ν_P (−)	Viscosity	Source
Salt	Zechstein (Permian)	Rock salt	2200	30000	0.25	Linear: 10^{16} to 10^{20} Pa s (cf., Table 1)	Lang et al. (2014)
Salt	Zechstein (Permian)	Rock salt	2150	25000	0.27	Power-law (BGRa): adjusted to temperatures of 325 to 400 K (cf., Table 1)	Liu et al. (2017); Bertrams et al. (2020)
Internal layer	Zechstein (Permian)	Anhydrite	2800	30000	0.23	Linear: 10^{23} Pa s	Liu et al. (2017); Bertrams et al. (2020)
Internal layer	Zechstein (Permian)	Potassium salt	1700	17000	0.28	Linear: $3.5*10^{13}$ Pa s	Liu et al. (2017); Bertrams et al. (2020)

continue for the complete loading phase, reach a maximum or may be followed by another reversal of the movement direction (Figs. 6, 7). The maximum downwards displacement represents an equilibrium state that is controlled by the viscosity of the salt and the elasticity of the surrounding materials. The observed maximum subsidence ranged from -0.6 to -11.4 m. In the lower part of the diapir, some upwards displacement occurs during complete loading, which is related to inflow from the salt-source layer on both sides (Fig. 6a, c).

The retreat of the ice sheet leads to another change of the movement directions (Figs. 5, 6, 7, 8; steps GR-1, GR-2, GR-3 and IG) and the previous subsidence at the surface is largely compensated. The compensation of the previous deformation is related to the load applied to the salt source layer by the retreating ice sheet and the elasticity of the supra-salt rocks, which restore the original shape after unloading. Lateral salt flow due to the ice load applied

onto the source layer only has a minor impact that can be observed when the ice margin is located at the centre of the model (step GR-2). The extracted curves display a change in the uplift rate during this step (Fig. 7).

The remaining deformation at the end of the runs depends on the choice of the material parameters. Some runs end with a stationary state, while in other runs a stationary state is not yet attained, even if the duration of the load-free step is doubled to 20000 a (Fig. 9a). In both cases the displacements at the end of the runs may be positive (i.e., uplift), negative (i.e., subsidence) or zero, ranging from 0.5 to − 0.4 m.

Models with only partial ice coverage during the maximum ice extent display a different behaviour. The salt diapir is free to rise due to lateral salt flow from the source layer as long as the ice margin is located next to the diapir (Fig. 9b). The uplift at the top of the diapir ranged from 0.5 to 2.8 m and was limited by the elasticity of the materials due to the lack of plasticity.
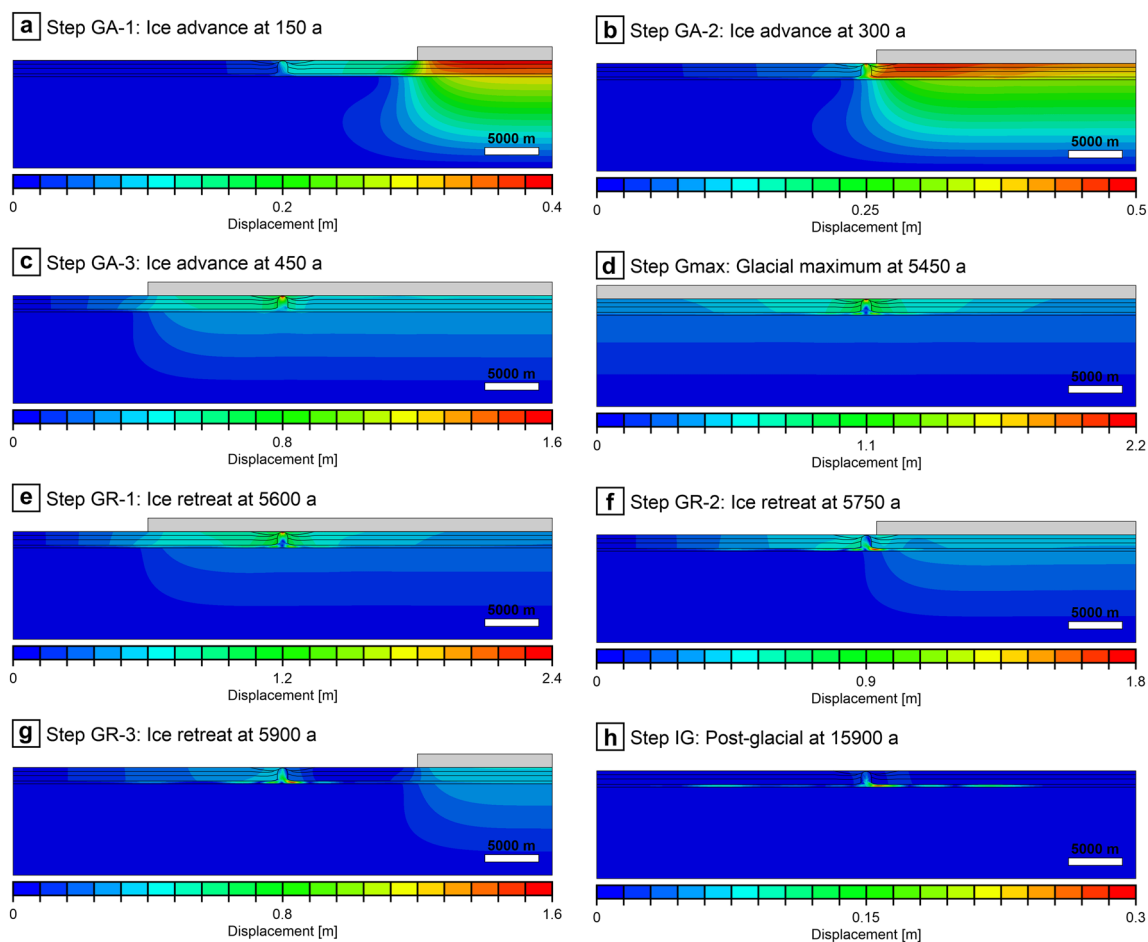
Fig. 5 Displacements in the model section during one complete run. The sections are from a model with a simple salt diapir and salt-source layer, linear viscous salt (10^{18} Pa s) and elastic parameter set "LA" (run BM-A11). The displacements are the total displacements at the end of the respective steps. Only the magnitudes of the displacement are shown, the direction of the displacement is not indicated. The grey bar on top of the sections indicates the extent of the ice sheet. **a–c** Ice advance. **d** Glacial maximum. **e–g** Ice retreat. **h** Post-glacial
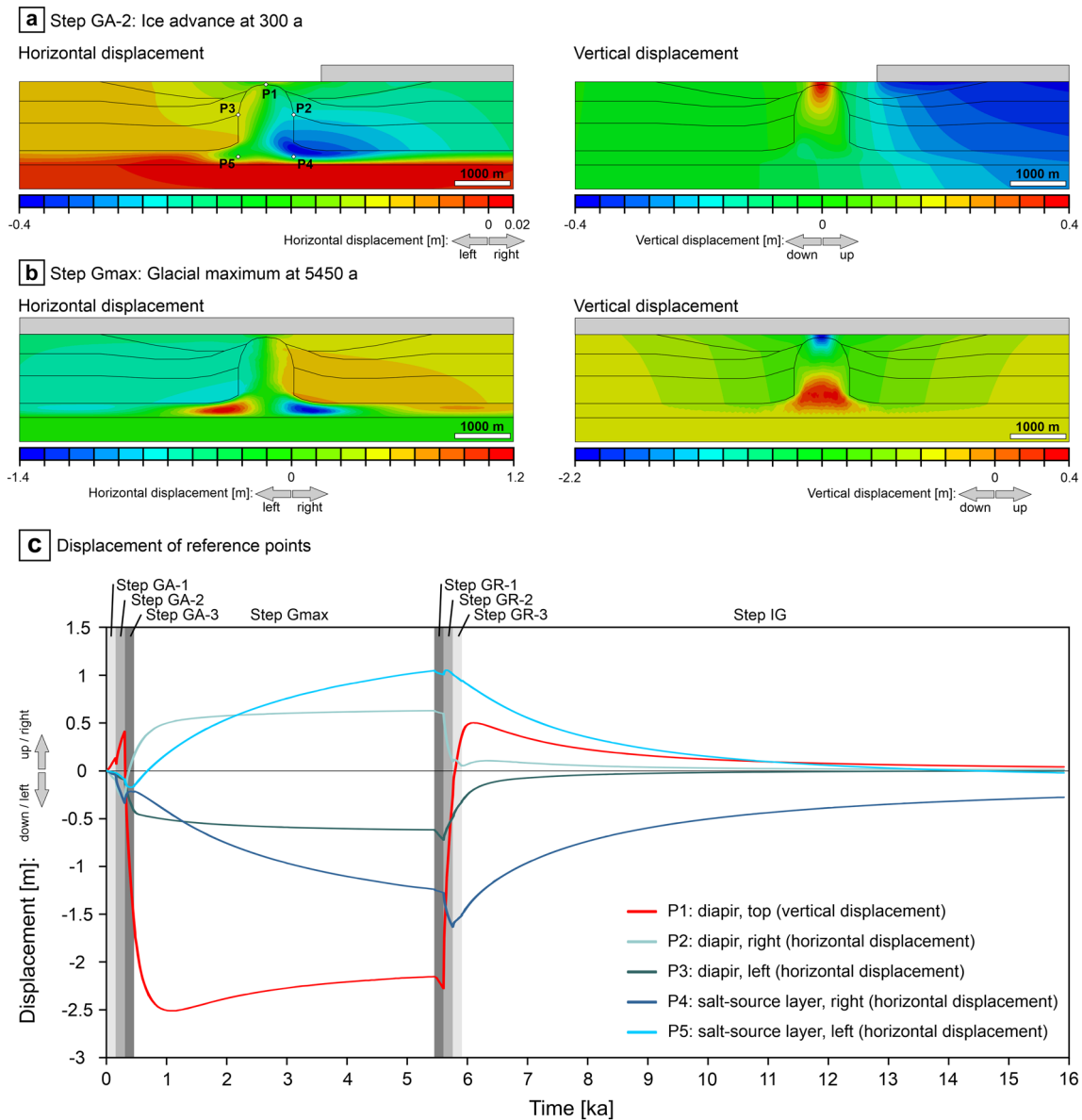
Fig. 6 Detail from the model section shown in Fig. 5 (run BM-A11). Positive displacement is upwards for the vertical component and to the right for the horizontal component, always representing total displacements at the ends of the respective steps. Negative displacement is downwards for the vertical component and to the left for the horizontal component. **a** Horizontal (left) and vertical (right) displacement during the ice advance (Step GA-2). The white points P1 to P5 indicate the locations of the reference points for the extracted displacements shown in (**b**). **b** Horizontal (left) and vertical (right) displacement during complete ice coverage (Step Gmax). **c** Temporal evolution of displacements extracted at reference points P1 to P5. The displacement of P1 at the top of the diapir is vertical, P2 to P5 show horizontal displacements. The locations of the reference points are indicated in (**a**) (left panel)

Linear and non-linear viscosity

The choice of a linear or non-linear viscous model for the salt rheology and the selected values has a large impact on the modelling results. In simulations with a non-linear viscous salt, the attained maximum displacements and the displacement rates are always distinctly lower and the largest part of the deformation can actually be attributed to the elasticity of the materials (Figs.7a, b, 8a). After unloading,

the deformation is not fully restored by the elasticity of the overlying rocks, typically causing some remnant subsidence above the diapir. Different values were tested for the pre-exponential parameter defining non-linear creep, corresponding to different temperatures. The differences in the resulting displacements and displacement rates are, however, quite small (Fig. 7b). In configurations with partial ice coverage, the downwards displacement of the complete model surface due to the elasticity clearly exceeds the rise of the

Fig. 7 Temporal evolution of the vertical displacement at the crest of the salt diapir. The diapir has a laterally extensive salt-source layer (cf., Fig. 4b). Steps of the ice advance (GA-1, GA-2, GA-3) and retreat (GR-1, GR-2, GR-3) have a duration of 150 a per step. The glacial maximum (Gmax) and post-glacial (IG) steps have durations of 5000 and 10000 a, respectively. **a** Salt diapir with source layer: comparison of linear viscous (10^18 Pa*s) and non-linear viscous (BGRa at 325 K) salt and elastic parameter sets "La" and "RK". For comparison, the results of purely elastic models without viscous salt are also shown. **b** Salt diapir with source layer: comparison of different linear and non-linear viscous salt rheologies. The elastic parameter set was "LA" for all displayed curves
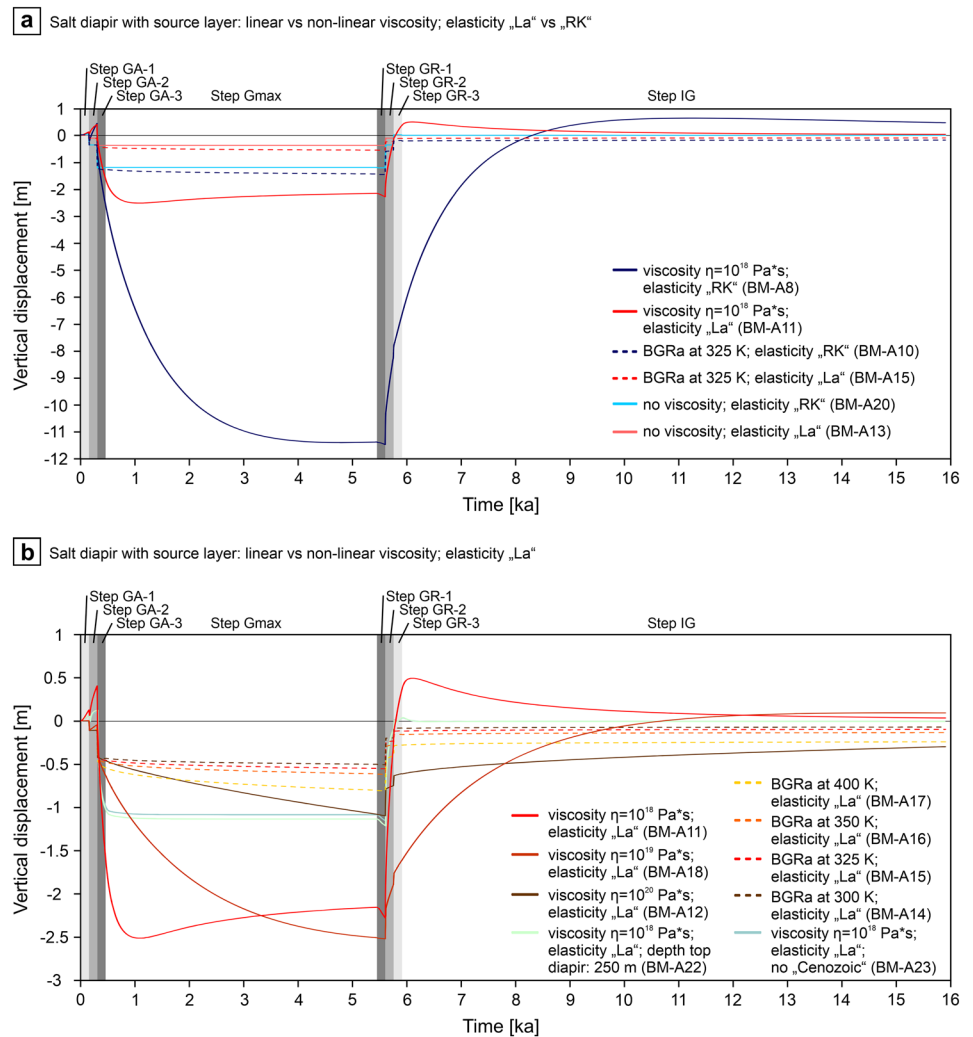
diapir due to lateral salt inflow, leading to net-subsidence during the loading phase (Fig. 9b).

In simulations with a linear viscous salt, the magnitude of the viscosity affects the maximum displacements and the shapes of the time-displacement curves. Lower viscosities cause higher maximum displacements (Fig. 7b). At the lowest tested viscosity, the sense of the displacement changes during the maximum loading phase as viscous and elastic deformation attain an equilibrium state. After unloading, displacements are restored by the elasticity of the supra-salt rocks. Remnant displacements at the end of the model runs were very low. In some models, the compensation was not completed at the end of the runs (Fig. 7). Even an extension of the unloaded phase to 20000 a did not allow for a complete compensation (Fig. 9a).

In addition to the displacement, the differential stress within the salt was extracted for three reference points. Reference points are located in the upper part of the diapir (centre of the section, 200 m below surface), the lower part of the diapir (centre of the section, 1100 m below surface)

and the salt-source layer (1000 m right from the centre, 1370 m below surface). For both linear and non-linear salt rheologies, the differential stress rapidly changes when the distribution of the load changes. Strong differences between linear and non-linear viscosities occur in the evolution of the differential stress during longer periods of constant loading (Fig. 10). Peaks of the differential stress are attained extremely rapidly during the first two phases of ice advance (GA-1 and GA-2). The peaks are generally lower in models applying linear viscosities than in those applying non-linear viscosities, as could be expected from the relation of the stress and the strain rate (Fig. 2). The attained peaks are followed by exponential-style decreases of the differential stress during further ice advance and complete ice coverage (GA-3 and Gmax). In simulations with a non-linear viscous salt, the differential stress decreases to minimum values that are clearly above zero (Fig. 10b). In contrast, linear viscous salt displays very rapid drops of the differential stress to values close to zero and the values remain very low until the loading conditions change during ice retreat (Fig. 10a).

Fig. 8 Temporal evolution of the vertical displacement at the crest of a salt diapir without source layer (cf., Fig. 4c). Steps of the ice advance (GA-1, GA-2, GA-3) and retreat (GR-1, GR-2, GR-3) have a duration of 150 a per step. The glacial maximum (Gmax) and post-glacial (IG) steps have durations of 5000 and 10000 a, respectively. **a** Salt diapir without source layer, no internal layers. Results for linear and non-linear viscous salt and elastic parameter sets "LA" and "RK" are compared. **b** Salt diapir without internal layers compared to salt structure with low-viscosity layers, representing potassium salt, and high-viscosity layers, representing anhydrite

a Salt diapir without source layer: linear vs non-linear viscosity; elasticity „La" vs „RK"

b Salt diapir without source layer and with internal layers
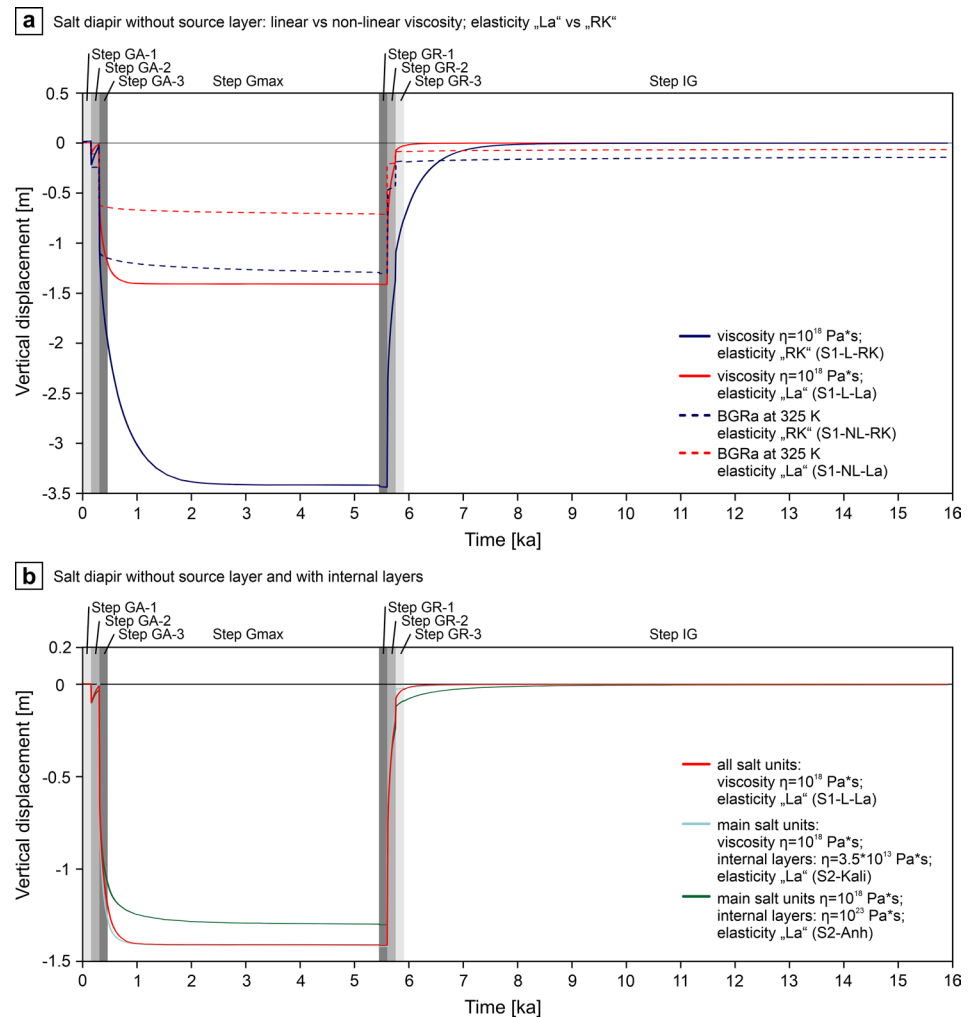
The first two phases of ice retreat (GR-1 and GR-2) again trigger a rapid rise of the differential stress, which is again followed by exponential-style decrease during further ice retreat and the load-free phase (GR-3 and IG). The minimum values attained in models with non-linear salt remain clearly above zero even after 10000 a without load (Fig. 10b), while for linear viscous salt the differential stress decreases to near zero (Fig. 10a).

Elastic parameters

The choice of the elastic parameters strongly affects the results of the simulations. Lower Young's moduli (i.e., higher elasticity) generally lead to higher displacements (Figs. 7a, b, 8a). During the maximum loading phases, the subsidence above the diapir is larger and it takes longer to attain the maximum values as the viscosity (load and time dependent) works against the elasticity (load dependent/time independent) in the subsidence phase. For a linear viscosity of 10^{18} Pa s, a maximum subsidence of -2.5 m is attained after 1050 a for parameter set "LA" (BM-A11), while for

parameter set "RK" (BM-A8) a maximum subsidence of -11.4 m is attained after 4800 a (Fig. 7a).

After the removal of the load, models with higher elasticity (i.e., lower Young's moduli) require more time to return to the original shape. The displacement may not be fully compensated even 20000 a after the removal of the load (Fig. 9a). For a linear viscosity of 10^{18} Pa*s the remaining displacements after 20000 a are $+0.04$ m for parameter set "La" and $+0.47$ m for parameter set "RK", respectively. The larger remaining displacements show that materials with higher elasticities take longer to restore the displacement against the viscosity.

Geometry of the model section

The geometry controls the distribution of the different materials in the model sections and has thus a major impact on the results (Figs. 7, 8). The presence of an extensive salt-source layer allows for lateral salt flow even if the distance between the diapir and the ice load is large. In models with a more complex geometry, there is no uplift during step GA-1

Fig. 9 Plots of the temporal evolution of the vertical displacement at the crest of the diapir. **a** Salt diapir with source layer. The durations of the glacial maximum (Gmax) and post-glacial (IG) steps have been extended to 15000 and 20000 a, respectively. Results for linear and non-linear viscous salt and elastic parameter sets "La" and "RK" are compared. **b** Salt diapir with source layer in an ice-marginal position. Results for linear and non-linear viscous salt and elastic parameter sets "La" and "RK" are compared. The glacial maximum (Gmax) and post-glacial (IG) steps have durations 10000 a each
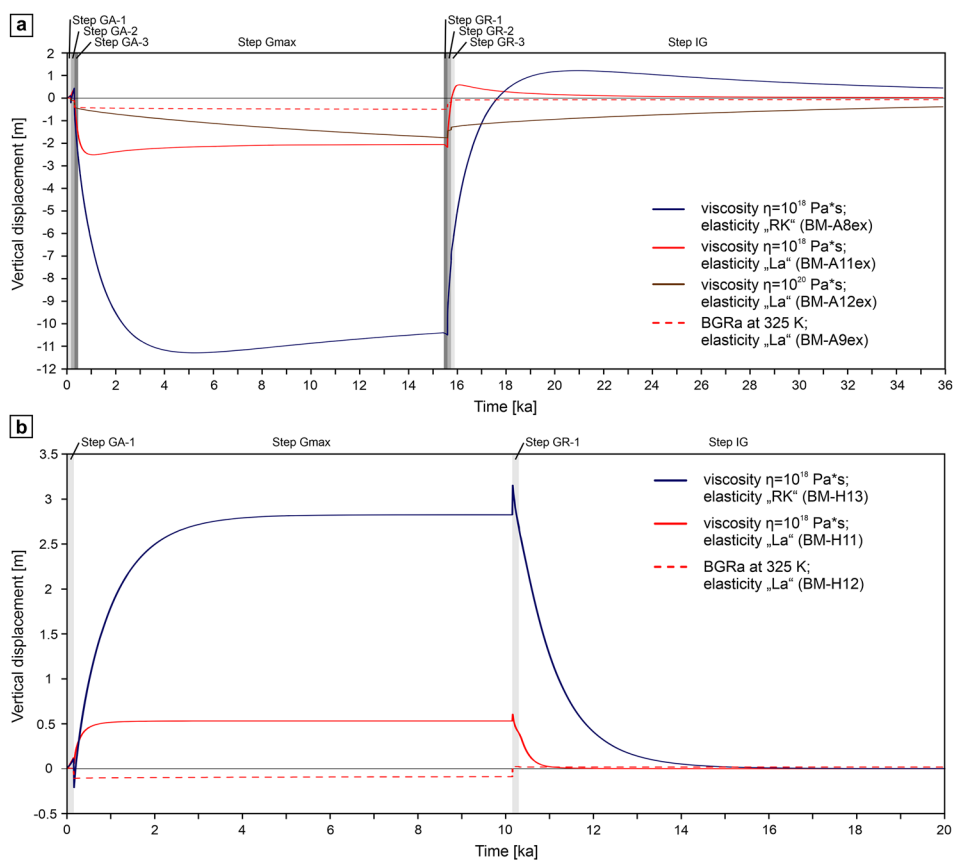
due to the lack of a salt-source layer. Some uplift may occur when the ice margin is located next to the diapir during step GA-2 (Figs. 5b, 6a, 8a, b). The subsidence above the diapir during full ice coverage is also lower than in models with a laterally extensive salt-source layer. The presence of internal layers of contrasting rheologies within the diapir has some impact on the results (Fig. 8). In models with higher-viscosity internal layers, the maximum displacements and the rates of viscous movement are lower than in models without internal layers. In contrast, the effect of lower-viscosity internal layers on the displacement is very small (Fig. 8b). In one run, the depth to the top of the diapir was increased to 250 m (Run BM-A22; Fig. 7b). The increase in thickness above the diapir reduced the maximum subsidence and the uplift, compared with the maxima attained in simulations with a 50-m-deep diapir.

Discussion

The model results are discussed with regard to the impact of the tested rheologies, focusing on the impact of linear vs non-linear viscous behaviour of the salt rocks and of the elasticity of the supra-salt rocks. Furthermore, we will

explore which additional parameters should be included in future models to attain more realistic results.

Qualitatively, the results of all model runs are similar and concur with those of previous conceptual (Liskowski 1993; Sirocko et al. 2008) and numerical models (Kock et al. 2012; Kock 2013; Lang et al. 2014). Quantitatively, the model results were controlled by the spatial and temporal change of the loading conditions and the viscosity and elasticity of the materials. During partial loading of the model surface (i.e., ice advance and retreat), salt flow from ice-covered to ice-free sections occurred in response to differential loading (Fig. 6a, c). The load applied onto the salt-source layer caused lateral salt flow into the diapir, resulting in uplift above the diapir (Fig. 11a). Lateral salt flow and uplift of the diapir were clearly observed in models applying a linear viscosity. If non-linear viscosity is applied, the uplift was very low. The maximum observed uplift was 2.8 m for linear viscous salt and 0.5 m for non-linear viscous salt, respectively. As no plasticity was included in the models, the maximum uplift was controlled by the elasticity of the supra-salt rocks (Fig. 9b).

During complete ice coverage, subsidence above the diapir occurred due to downwards displacement and broadening of the diapir (Figs. 6b, c, 11b). In the lower part of the diapir, some upwards displacement occurred due to lateral inflow

Fig. 10 Plots of the temporal evolution of the differential stress, comparing the effects of linear and non-linear salt rheology. **a** Evolution of the differential stress for linear viscous salt (viscosity $\eta = 10.^{18}$ Pa*s; elasticity „LA"; run BM-A11). Data are plotted for the upper part of the salt diapir (centre of the section, 200 m below surface), the lower part of the salt diapir (centre of the section, 1,100 m below surface) and the salt-source layer (1000 m right from the centre, 1,370 m below surface). **b** Evolution of the differential stress for non-linear viscous salt (BGRa at 325 K; elasticity "LA"; run BM-A15). Data are plotted for the upper part of the salt diapir (centre of the section, 200 m below surface), the lower part of the salt diapir (centre of the section, 1100 m below surface) and the salt-source layer (1000 m right from the centre, 1370 m below surface)
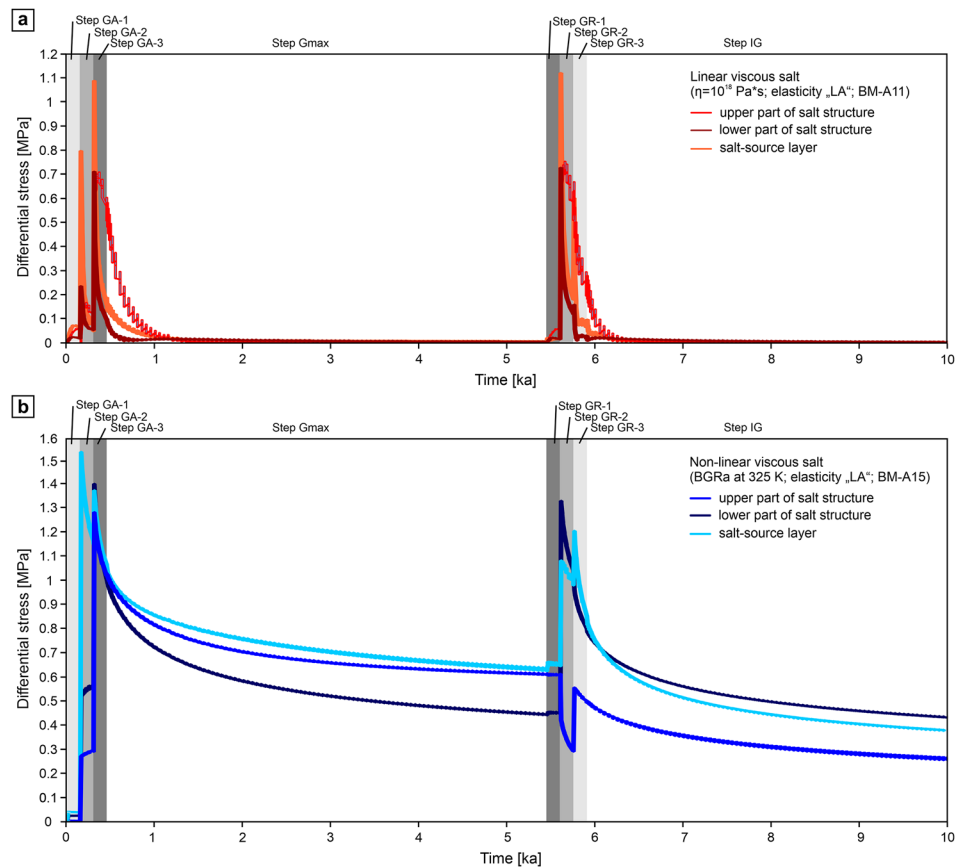
from the source layer from both sides. In the central part of the diapir, the displacement remained very low (Fig. 6b). Such different directions and magnitudes of displacement indicate complex stress and strain patterns within a salt diapir that should be considered when aiming for predictive models.

The downwards displacement of the upper part of diapir and subsidence at the surface during complete ice coverage may seem counterintuitive, as the pressure load applied by the ice sheet is the same everywhere along the model section. The salt movement can thus not be driven by a stress gradient due to differential loading. Instead, deformation is controlled by different ratios between vertical and horizontal stress in elastic (supra-salt rocks) and viscoelastic (salt) materials. In elastic materials, the horizontal stress is related to the vertical stress by the Poisson's ratio. The vertical stress is thus always larger than the horizontal stress. In viscoelastic materials, the horizontal stress approaches the vertical stress after a relatively short period of loading. The length of this period depends on the viscosity (< 10 a for the parameters involved in this study). Therefore, the horizontal stress becomes larger in the viscoelastic salt than in the elastic supra-salt rocks, allowing for a broadening of the salt diapir at the expense of the supra-salt rocks. The maximum

subsidence above the diapir ranged from -0.6 m to -11.4 m, depending on the viscosity of the salt and the elasticity of the supra-salt rocks (Fig. 7a). Larger deformation is favoured by lower values of Young's modulus in the supra-salt rocks and lower viscosity of the salt (Fig. 11b). The viscosity (load and time dependent) controls the subsidence rate as it works against instant (load dependent/time independent) elastic deformation. The restoration of the deformation after unloading is controlled by the elastic properties of the supra-salt rocks. The maximum possible deformation in the model is controlled by the ratio of the viscosity of the salt and the elasticity of the supra-salt rocks. Due to the complexity of the model, however, the absolute impact of these factors cannot be defined.

The obtained displacements may seem low in relation to the dimensions of the model section and the minimum element-edge lengths. However, the finite-element method does not require the mesh resolution to be in the range of the expected displacements to obtain valid results (Fagan 1992; Zienkiewicz and Taylor 2005). Instead, element-edge lengths can be much larger than the expected displacements (cf., Hampel et al. 2019).
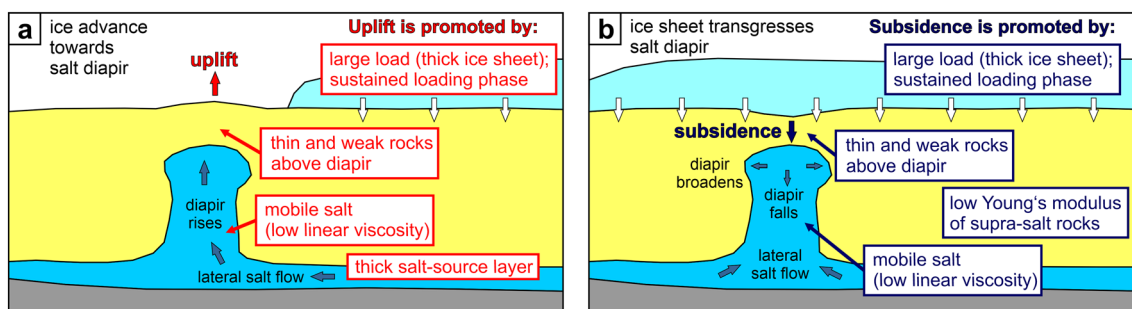
Fig. 11 Summary of the model results. **a** An ice advance towards the salt diapir causes surface uplift above the diapir due to lateral salt flow and diapiric rise. **b** Ice coverage of the salt diapir causes subsidence above the salt diapir due to falling and broadening of the diapir

The rheology of salt rocks

The deformation of salt rocks is dominated by non-linear dislocation creep at high stress, while linear solution-precipitation creep dominates under low stress conditions (Hunsche and Schulze 1994; Urai et al. 1986; Schléder and Urai 2005; Lüdeling et al. 2022). The rheology of rock salt that deforms at low stress and strain rates, however, is not yet properly validated by experimental data and an area of ongoing research (Li et al. 2012; Li and Urai 2016; Bérest et al. 2019; Lüdeling et al. 2022). At geologically relevant stress levels, temperatures and time scales, salt rheology is at the transition between linear and non-linear viscosity (van Keken et al. 1993; Herchen et al. 2018; Bérest et al. 2019). Geological studies on the long-term evolution of salt-bearing basins or entire salt structures generally apply a linear viscosity, commonly using the same viscosity for the entire salt body (Gemmer et al. 2004, 2005; Nikolinakou et al. 2012, 2014). Very few studies have used stratified salt units with different viscosities (e.g., Albertz and Ings 2012) or compared linear and non-linear viscosities (e.g., Li et al. 2012; Herchen et al. 2018; Granado et al. 2021). Estimates of the viscosity of natural salt bodies span several orders of magnitude (Weijermars et al. 1993; Mukherjee et al. 2010; Rowan et al. 2019) and can thus not provide the input parameters required for higher-resolution numerical models.

Laboratory studies, which generally are conducted in short time, at high differential stress and with dry salt-rock samples, indicate that the rheology of salt is represented by a power-law viscosity (Bérest et al. 2019; Lüdeling et al. 2022). An extensive database of the relevant material parameters for different salt-rock lithologies exists (e.g., Hunsche and Hampel 1999; Hunsche et al. 2003; Bräuer et al. 2011), which are widely used as input for high-resolution numerical models (e.g., Kock et al. 2012; Liu et al. 2017; Bertrams et al. 2020). In contrast, few experimental data exist on the behaviour of salt-rock samples at low stress levels and strain rates. Compilations of stress versus strain rate plots using available experimentally derived data suggest that creep at differential stresses below 5 MPa is linear, while creep at differential stresses above 5 MPa follows a power-law with an exponent between 3 and 7 (Herchen et al. 2018; Bérest et al. 2019; Lüdeling et al. 2022). The magnitude of the stress at the transition is temperature dependant, requiring higher stresses at lower temperatures (Herchen et al. 2018).

In the presented models, the displacements are always larger in models with linear viscous salt than in those applying non-linear viscosity (Figs. 7, 8, 9). The differential stress caused by the 300-m-thick ice sheet within the salt unit is generally less than 2 MPa (Fig. 10). At this magnitude of differential stress, a linear viscous behaviour of the salt seems thus realistic (Herchen et al. 2018; Bérest et al. 2019; Zill et al. 2022). The simplification of salt rheology to linear viscous behaviour is appropriate in geological models focused on the long-term evolution of salt structures and their interaction with the supra-salt rocks and earth-surface processes. Considering salt rocks as linear viscous is an established practice in geological models that has been applied in a large number of studies, successfully reconstructing the geometries observed in natural salt structures and their supra-salt rocks (e.g., Gemmer et al. 2004, 2005; Albertz and Ings 2012; Nikolinakou et al. 2012, 2014; Rowan et al. 2019; Granado et al. 2021). More sophisticated rheological models are required in studies aiming at the internal behaviour of salt structures, especially with regard to the stability of underground workings, caverns or waste repositories. Complex stress and deformation patterns occur within natural salt structures, locally causing much higher stresses. In such models, the deformation of salt rocks is commonly decomposed into the contributions from linear solution-precipitation and non-linear dislocation creep (cf., Spiers et al. 1990). The application of such combined descriptions of salt rheology commonly applied in numerical modelling (e.g., Spiers and Carter 1998; Urai and Spiers 2007; Baumann et al. 2022; Zill et al. 2022). Zill et al. (2022) also modelled the response of salt structures to ice-sheet loading. Their results showed that a model combining linear and non-linear salt creep results in ~5 times more uplift of the salt structure

than a model applying only the non-linear BGRa creep (Zill et al. 2022).

Natural salt structures display complex internal architectures, comprising a variety of salt rocks and non-salt rocks with contrasting mechanical properties (Hudec and Jackson 2007; Rowan et al. 2019). Even the incorporation of two relatively thin internal layers significantly affected the model results (Fig. 8b). Regional studies aimed at specific salt structures, therefore, need to better resolve the internal architecture to make realistic predictions of ice-load induced deformation. A rich, experimentally derived database of fitting parameters exists for power-law creep of different salt lithologies at high differential stresses (e.g., Hunsche et al. 2003; Bräuer et al. 2011; Liu et al. 2017). In contrast, linear viscous behaviour of different salt lithologies is less well constrained, as experimental data on creep at low differential stresses are rare (Bérest et al. 2019; Lüdeling et al. 2022). Assigning the appropriate linear viscosities when modelling heterogeneous salt comprising various lithologies remains thus challenging.

The impact of elasticity

The presented models demonstrate that the choice of elastic parameters may strongly impact the model results (Fig. 7a). Usually, the elastic behaviour of materials receives far less consideration than viscous or creep behaviour. In models concerned with long-term processes and non-transient loads, where the elasticity has a minor impact, this may be appropriate. The strong impact of the elasticity in the presented models is caused by the rapid and repeated redistribution of the ice load at the model surface. Young's moduli in parameter set "LA" are higher than in parameter set "RK" (Tables 2, 3). The ratio is about 3:1 for the Palaeozoic and Mesozoic rocks and 10:1 for the Cenozoic rocks. Lower values of Young's modulus allow for larger elastic displacements and vice versa. Parameter sets "LA" (Lang et al. 2014) and "RK" (Liu et al. 2017; Bertrams et al. 2020) are both compiled from several studies on the mechanical properties of the various lithostratigraphic units in the Central European Basin System (Tables 2, 3). The wide spread of the values can be explained by the heterogeneous nature of the lithostratigraphic units. The applied values are, however, in the range for generic geological materials (e.g., Turcotte and Schubert 2002). The results demonstrate that a careful choice of the elastic parameters for numerical modelling studies is required, if transient loads are involved.

Towards more realistic models

As in every numerical model, a number of simplifications was required for feasibility and focus on the main questions. The geometry of the model section is relatively complex

to depict the architecture around existing salt structures (Figs. 1d, 4). However, with the exception of the Cenozoic infill of the rim synclines, the material parameters of the supra-salt rocks are very similar (Tables 2, 3). Interactions between real salt structures and ice sheets may be further complicated due to 3D effects, especially if salt structures are strongly asymmetric or have an elongated shape. The yield strength of the modelled rocks was deliberately ignored to avoid plastic deformation, which would have hampered the evaluation of the relative importance of the viscosity and elasticity. As shown in earlier models, including plastic behaviour affects the displacements remaining at the end of a model run but does not change the style of the deformation (cf., Lang et al. 2014). Especially poorly consolidated, mechanically weak rocks, as the infill of the rim synclines can be expected to deform plastically. In contrast, the load of an ice sheet may be insufficient to trigger permanent deformation in well-consolidated, mechanically strong rocks. If deformation due to ice-sheet loading occurs in such rocks, it is generally restricted to pre-existing weaknesses (Hampel et al. 2009, 2010; Brandes et al. 2015). To obtain more realistic magnitudes of the displacements, however, the yield strength of the materials needs to be considered. Furthermore, previous models (Lang et al. 2014) displayed intense plastic deformation in the weak uppermost model unit at the locations of the ice margins. Deformation of near-surface unconsolidated deposits by the weight of an ice sheet is a well-known process (e.g., Andersen et al. 2005; Aber & Ber 2007), but outside the scope of this study. Furthermore, the deformation patterns in the uppermost model units at the ice margin observed by Lang et al. (2014) were partly unrealistic and did not resemble any natural deformation structures (cf., Andersen et al. 2005; Aber and Ber 2007).

Both dislocation creep and solution-precipitation creep of salt rock are temperature-dependant processes (Fig. 2; Van Keken et al. 1993; Urai et al. 2008). Models including the temperature as a boundary condition need to consider variations due to the geothermal gradient and the thermal conductivity of the different lithologies. Furthermore, the surface temperature and, with some time lag, the temperature in the subsurface dramatically change during the course of a full glacial cycle, culminating in the spatially and temporarily variable formation of permafrost. Existing models show that the temperature change during a glacial cycle may impact the behaviour of a salt structure (Kock et al. 2012).

Studies of ice-load induced deformation have primarily focussed on the effect of long-wavelength lithospheric flexure and isostatic rebound caused by glacial loading and postglacial unloading (e.g., Stewart et al. 2000; Hampel et al. 2009, 2010; Brandes et al. 2015). Glacial isostatic adjustment is characterised by subsidence below the ice sheet, which is compensated by post-glacial uplift. A forebulge is formed in a certain distance from the ice margin,

which is uplifted during glacial loading and subsides during unloading (Walcott 1970; Stewart et al. 2000). Glacial isostatic adjustment is not included in the presented models, as such long-wavelength processes act at very different spatial scales and thus require a very different model set-up. However, glacial isostatic adjustment may affect ice-load driven salt movement by basin-scale tilting of the salt-source layer and by stress changes due to lithospheric flexure. Tilting of the salt-source layer causes an elevation head that can trigger downslope gliding of the salt and overlying rocks (Hudec and Jackson 2007; Brun and Fort 2011). Although gliding may occur at low slopes, gliding at slopes of less than 1° requires basin widths, i.e., lateral extents of the salt-source layer, of 200–400 km (Brun and Fort 2011). Based on the models of the glacial isostatic depression beneath the Fennoscandian ice sheet (Talbot 1999; Stewart et al. 2000; Steffen and Wu 2011) the large-scale tilt would generally be lower than 0.1°. Løtveit et al. (2019) modelled the tilt in the forebulge area, suggesting that maximum values of ~0.2° may occur. The potential tilting of the salt-source layer by glacial isostatic adjustment and the lateral extent of the salt-source layer are thus probably too low to have a significant effect on the deformation. In model set-ups lacking a laterally extensive salt-source layer, there should be no effect at all. Stress changes induced by lithospheric flexure due to glacial isostatic adjustment probably have a rather low impact on the deformation of salt structures. Ice load-induced deformation of salt structures mainly occurs when the salt structure is in an ice-marginal position. In contrast, the highest stresses due to glacial isostatic adjustment occur either beneath the centre of the ice shield or in the area of the forebulge, tens to hundreds of kilometres outside the ice margin (Stewart et al. 2000; Hampel et al. 2009, 2010; Brandes et al. 2015). Tilting and stress changes induced by glacial isostatic adjustment may, however, be included in future models to test their impact. For the present study, the focus is on the effects of the material properties and tilting or stress changes due to glacial isostatic adjustment were thus not considered.

This study was intended primarily as a parameter study and was not aimed at reproducing any real-world situations. The deformation observed in the models is generally lower than measurements or estimates from field observations, which commonly indicate several tens of metres of displacement (cf., Sirocko et al. 2002; Stackebrandt 2005, 2016; Müller and Obst 2008; Al Hseinat et al. 2016; Hardt et al. 2021). The discrepancy between models and field observations was already observed in a previous modelling study by Lang et al. (2014). The impact of ice-sheet loading on the salt structures during the Pleistocene glaciations has probably been overestimated. When analysing the Pleistocene or Holocene salt movement, it is therefore important to consider how the studied salt structures behave under the respective geological conditions, especially with regard to the stress field, basin dynamics and sedimentation patterns. Displacements triggered solely by ice-sheet loading are generally low and probably insufficient to explain the larger deformation inferred from some field observations.

Conclusions

Our new modelling results highlight the impact of the rheology on the resulting deformation, both with regard to the viscosity and elasticity. In general, our results support previous conceptual (Liszkowski 1993; Sirocko et al. 2008) and numerical models (Kock et al. 2012; Kock 2013; Lang et al. 2014; Zill et al. 2022). In all conducted simulations, the load of the ice sheet triggers lateral and vertical salt flow, finally resulting in uplift or subsidence above the salt diapir in the centre of the model section. The location of the ice margin relative to the diapir exerts the first-order control on the style of the response of the diapir to ice-sheet loading. Uplift occurs if the load is only applied to the surface above the salt-source layer, causing lateral salt flow into the diapir. If load is applied to the surface above the top of the diapir, the diapir is pushed down and subsidence occurs. The downwards movement of the diapir is accompanied by a slight broadening at the expense of the surrounding supra-salt rocks. The maximum downwards displacement of the diapir is limited by the elasticity of the supra-salt rocks. After the removal of the ice load, the attained displacements are largely compensated by the elasticity of the supra-salt rocks, as no plasticity was included.

The directions and magnitudes of the displacements depend on the model geometry, the viscosity and the elasticity of the modelled materials. The results highlight the importance of a cautious parameter choice for both the viscous and elastic behaviour of the modelled materials. Model sections with extensive salt-source layers generally allow for larger displacements than those with a lateral pinch-out of the salt. The presence of more competent layers within the salt diapir also reduces the displacement.

The viscosity of the salt has a major impact on the model results. Linear viscous salt is more mobile than power-law viscous salt and thus allows for larger displacements. Furthermore, the range of the resulting displacements is far wider, if linear viscosity is applied. The use of a linear viscous salt rheology seems appropriate for the boundary conditions applied in this model, where the differential stress caused by a 300-metres-thick ice sheet is low, the time scale for the deformation is several thousands of years and the focus of the study is on the behaviour of the entire salt diapir and the interactions with the supra-salt rocks and earth-surface processes.

The choice of the elastic parameters of the modelled materials has a large impact on model results that may even exceed the impact of the viscosity. More elastic materials (i.e., lower Young's modulus) allow for larger displacements in all modelling steps. The role of elasticity is commonly neglected in large-scale models of geological processes. The results clearly show that a careful choice of the elastic parameters for numerical modelling studies is required, if transient loads are involved.

Declarations

References

Aber JS, Ber A (2007) Glaciotectonism. Dev Quat Sci 6:1–246

Al Hseinat M, Hübscher C, Lang J, Lüdmann T, Ott I, Polom U (2016) Triassic to recent tectonic evolution of a crestal collapse graben above a salt-cored anticline in the Glückstadt Graben/North German Basin. Tectonophys 680:50–66. https://doi.org/10.1016/j.tecto.2016.05.008

Albertz M, Ings SJ (2012) Some consequences of mechanical stratification in basin-scale numerical models of passive-margin salt tectonics. Geol Soc Lond Spec Publ 363:303–330. https://doi.org/10.1144/SP363.14

Andersen LT, Hansen DL, Huuse M (2005) Numerical modelling of thrust structures in unconsolidated sediments: implications for glaciotectonic deformation. J Struc Geol 27:587–596. https://doi.org/10.1016/j.jsg.2005.01.005

Baldschuhn R, Binot F, Fleig S, Kockel F (1996) Geotektonischer atlas von nordwest-deutschland und dem deutschen nordsee-sektor. Geol Jahrb A 153:1–55

Baumann TS, Kaus B, Popov A, Urai J (2022) Modeling of the 3D stress state of typical salt formations. In: de Bresser JHP, Drury MR, Fokker PA, Gazzani M, Hangx SJT, Niemeijer AR, Spiers CJ (eds) The mechanical behavior of salt X. CRC Press, pp 363–371

Beaud F, Flowers GE, Venditti JG (2016) Efficacy of bedrock erosion by subglacial water flow. Earth Surf Dyn 4:125–145. https://doi.org/10.5194/esurf-4-125-2016

Benn DI, Hulton NRJ (2010) An Excel™ spreadsheet program for reconstructing the surface profile of former mountain glaciers and ice caps. Comp Geosci 36:605–610. https://doi.org/10.1016/j.cageo.2009.09.016

Bérest P, Gharbi H, Brouard B, Brückner D, DeVries K, Hévin G, Hofer G, Spiers C, Urai J (2019) Very slow creep tests on salt samples. Rock Mech Rock Eng 52:2917–2934. https://doi.org/10.1007/s00603-019-01778-9

Bertrams N, Bollingerfehr W, Eickemeier R, Fahland S, Flügge J, Frenzel B, Hammer J, Kindlein J, Liu W, Maßmann J, Mayer KM, Mönig J, Mrugalla S, Müller-Hoeppe N, Reinhold K, Rübel A, Schubarth-Engelschall N, Simo E, Thiedau J, Thiemeyer T, Weber JR, Wolf J (2020) RESUS Grundlagen zur Bewertung eines Endlagersystems in steil lagernden Salzformationen. Gesellschaft für Anlagen- und Reaktorsicherheit (GRS), Köln

Brandes C, Pollok L, Schmidt C, Riegel W, Wilde V, Winsemann J (2012) Basin modelling of a lignite-bearing salt rim syncline: insights into rim syncline evolution and salt diapirism in NW Germany. Basin Res 24:699–716. https://doi.org/10.1111/j.1365-2117.2012.00544.x

Brandes C, Steffen H, Steffen R, Wu P (2015) Intraplate seismicity in northern Central Europe is induced by the last glaciation. Geology 43:611–614. https://doi.org/10.1130/G36710.1

Bräuer V, Eickemeier R, Eisenburger D, Grissemann C, Hesser J, Heusermann S, Kaiser D, Nipp HK, Nowak T, Plischke I, Schnier H, Schulze O, Sönnke J, Weber JR (2011) Description of the Gorleben site Part 4: geotechnical exploration of the Gorleben salt dome. Schweizerbart, Stuttgart

Brun JP, Fort X (2011) Salt tectonics at passive margins: Geology versus models. Mar Petrol Geol 28:1123–1145. https://doi.org/10.1016/j.marpetgeo.2011.03.004

Carter NL, Hansen FD (1983) Creep of rock salt. Tectonophys 92:275–333. https://doi.org/10.1016/0040-1951(83)90200-7

Carter NL, Hansen FD, Senseny PE (1982) Stress magnitudes in natural rock salt. J Geophys Res: Solid Earth 87:9289–9300. https://doi.org/10.1029/JB087iB11p09289

Cohen HA, Hardy S (1996) Numerical modelling of stratal architectures from differential loading of a mobile substratum. Geol Soc Lond Spec Publ 100:265–273. https://doi.org/10.1144/GSL.SP.1996.100.01.17

DEKORP-BASIN Research Group (1999) Deep crustal structure of the Northeast German basin: new DEKORP-BASIN'96 deep-profiling results. Geology 27:55–58. https://doi.org/10.1130/0091-7613(1999)027%3C0055:DCSOTN%3E2.3.CO;2

Doornenbal H, Stevenson A (2010) Petroleum geological Atlas of the Southern Permian basin Area. EAGE Publications, Houten

Ehlers J, Grube A, Stephan HJ, Wansa S (2011) Pleistocene glaciations of North Germany new results. In: Ehlers J, Gibbard PL, Hughes PD (eds) Quaternary Glaciations Extent and Chronology–a Closer Look. Dev Quat Sci 15. Elsevier, Amsterdam, pp 149–162

Fagan MJ (1992) Finite element analysis–theory and practice. Pearson Prentice Hall, London

Fossen H (2016) Structural geology. Cambridge University Press, Cambridge

Gemmer L, Ings SJ, Medvedev S, Beaumont C (2004) Salt tectonics driven by differential sediment loading: stability analysis and finite-element experiments. Basin Res 16:199–218. https://doi.org/10.1111/j.1365-2117.2004.00229.x

Gemmer L, Beaumont C, Ings SJ (2005) Dynamic modelling of passive margin salt tectonics: effects of water loading, sediment properties and sedimentation patterns. Basin Res 17:383–402. https://doi.org/10.1111/j.1365-2117.2005.00274.x

Granado P, Ruh JB, Santolaria P, Strauss P, Muñoz JA (2021) Stretching and contraction of extensional basins with pre-rift salt: a numerical modelling approach. Front Earth Sci 9:648937. https://doi.org/10.3389/feart.2021.648937

Hampel A, Hetzel R, Maniatis G, Karow T (2009) Three-dimensional numerical modeling of slip rate variations on normal and thrust fault arrays during ice cap growth and melting. J Geophys Res Solid Earth. https://doi.org/10.1029/2008JB006113

Hampel A, Karow T, Maniatis G, Hetzel R (2010) Slip rate variations on faults during glacial loading and post-glacial unloading: implications for the viscosity structure of the lithosphere. J Geol Soc 167:385–399. https://doi.org/10.1144/0016-76492008-137

Hampel A, Lüke J, Krause T, Hetzel R (2019) Finite-element modelling of glacial isostatic adjustment (GIA): Use of elastic foundations at material boundaries versus the geometrically non-linear formulation. Comp Geosci 122:1–14. https://doi.org/10.1016/j.cageo.2018.08.002

Hardt J, Norden B, Bauer K, Toelle O, Krambach J (2021) Surface cracks – geomorphological indicators for late Quaternary halotectonic movements in Northern Germany. Earth Surf Processes Landforms 46:2963–2983. https://doi.org/10.1002/esp.5226

Henneberg M, Mertineit M, Hammer J, Zulauf G (2018) Fabric, paleostress and mineralogical composition of impure Rotliegend rock salt (North German Basin). In: Fahland S, Hammer J, Hansen F, Heusermann S, Lux K-H, Minkley W (eds) Mechanical Behavior of Salt (SaltMech IX). Federal Institute for Geosciences and Natural Resources (BGR), Hannover, pp 131–141

Henneberg M, Nowara P, Hammer J, Zulauf J, Zulauf G (2022) Depth-dependent variation of microfabrics and deformation mechanisms in bedded rock salt. ZDGG 173:167–191. https://doi.org/10.1127/zdgg/2

Herchen K, Popp T, Düsterloh U, Lux K-H, Salzer K, Lüdeling C, Günther R-M, Rölke C, Minkley W, Hampel A, Yildirim S, Staudtmeister K, Gährken A, Stahlmann J, Reedlunn B, Hansen FD (2018) WEIMOS: Laboratory investigations of damage reduction and creep at small deviatoric stresses in rock salt. In: Fahland S, Hammer J, Hansen F, Heusermann S, Lux K-H, Minkley W (eds) Mechanical Behavior of Salt (SaltMech IX). Federal Institute for Geosciences and Natural Resources (BGR), Hannover, pp 175–192

Hudec MR, Jackson MP (2007) Terra infirma: understanding salt tectonics. Earth-Sci Rev 82:1–28. https://doi.org/10.1016/j.earscirev.2007.01.001

Hughes AL, Gyllencreutz R, Lohne ØS, Mangerud J, Svendsen JI (2016) The last Eurasian ice sheets–a chronological database and time-slice reconstruction, DATED-1. Boreas 45:1–45. https://doi.org/10.1111/bor.12142

Hunsche U, Hampel A (1999) Rock salt–the mechanical properties of the host rock material for a radioactive waste repository. Eng Geol 52:271–291. https://doi.org/10.1016/S0013-7952(99)00011-3

Hunsche U, Schulze O (1994) Das Kriechverhalten von Steinsalz. Kali Und Steinsalz 11:238–255

Hunsche U, Schulze O, Walter F, Plischke I (2003) Thermomechanisches Verhalten von Salzgestein. Bundesanstalt für Geowissenschaften und Rohstoffe (BGR), Hannover

Jackson MPA, Talbot CJ (1986) External shapes, strain rates, and dynamics of salt structures. GSA Bull 97:305–323. https://doi.org/10.1130/0016-7606(1986)97%3C305:ESSRAD%3E2.0.CO;2

Jackson MPA, Vendeville BC (1994) Regional extension as a geologic trigger for diapirism. GSA Bull 106:57–73. https://doi.org/10.1130/0016-606(1994)106%3C0057:REAAGT%3E2.3.CO;2

Jackson MPA, Vendeville BC, Schultz-Ela DD (1994) Structural dynamics of salt systems. Ann Rev Earth Planet Sci 22:93–117

Jaritz W (1973) Zur Entstehung der Salzstrukturen Norddeutschlands. Geol Jahrb A 10:1–77

Kneuker T, Mertineit M, Schramm M, Hammer J, Zulauf G, Thiemeyer N (2018) Microfabrics and composition of Staßfurt and Leine rock salt (Upper Permian) of the Morsleben site (Germany): Constraints on deformation mechanisms and palaeodifferential stress. In: Fahland S, Hammer J, Hansen F, Heusermann S, Lux K-H, Minkley W (eds) Mechanical Behavior of Salt (SaltMech IX). Federal Institute for Geosciences and Natural Resources (BGR), Hannover, pp 143–157

Kock I (2013) Parameterstudie zur Gletscherüberfahrung und Integrität eines Salzdiapirs. Gesellschaft für Anlagen- und Reaktorsicherheit (GRS), Köln

Kock I, Eickemeier R, Frieling G, Heusermann S, Knauth M, Minkley W, Navarro M, Nipp HK, Vogel P (2012) Integritätsanalyse der geologischen Barriere–Bericht zu Arbeitspaket 91–Vorläufige Sicherheitsanalyse für den Standort Gorleben. Gesellschaft für Anlagen- und Reaktorsicherheit (GRS), Köln

Kockel F (2003) Inversion structures in central Europe e expressions and reasons, an open discussion. Neth J Geosci 82:367–382. https://doi.org/10.1017/s0016774600020187

Lambeck K, Purcell A, Zhao J, Svensson NO (2010) The Scandinavian ice sheet: from MIS 4 to the end of the last glacial maximum. Boreas 39:410–435. https://doi.org/10.1111/j.1502-3885.2010.00140.x

Lang J, Hampel A, Brandes C, Winsemann J (2014) Response of salt structures to ice-sheet loading: implications for ice-marginal and subglacial processes. Quat Sci Rev 101:217–233. https://doi.org/10.1016/j.quascirev.2014.07.022

Lang J, Lauer T, Winsemann J (2018) New age constraints for the Saalian glaciation in northern central Europe: Implications for the extent of ice sheets and related proglacial lake systems. Quat Sci Rev 180:240–259. https://doi.org/10.1016/j.quascirev.2017.11.029

Li SY, Urai JL (2016) Rheology of rock salt for salt tectonics modeling. Petrol Sci 13:712–724. https://doi.org/10.1007/s12182-016-0121-6

Li S, Abe S, Urai JL, Strozyk F, Kukla PA, Van Gent H (2012) A method to evaluate long-term rheology of Zechstein salt in the Tertiary. In: Bérest P, Ghoreychi M, Hadj-Hassen F, Tijani M (eds) Mechanical behavior of salt VII, Taylor & Francis Group. CRC Press, London

Liszkowski J (1993) The effects of Pleistocene ice-sheet loading-deloading cycles on the bedrock structure of Poland. Folia Quat 64:7–23

Liu W, Völkner E, Minkley W, Popp T (2017) Zusammenstellung der Materialparameter für THM-Modellberechnungen. Bundesanstalt für Geowissenschaften und Rohstoffe (BGR), Hannover

Løtveit IF, Fjeldskaar W, Sydnes M (2019) Tilting and flexural stresses in basins due to glaciations—An example from the Barents Sea. Geosci 9:474. https://doi.org/10.3390/geosciences9110474

Lüdeling C, Günther R-M, Hampel A, Sun-Kurczinski J, Wolters R, Düsterloh U, Lux K-H, Yildirim S, Zapf D, Wacker S, Epkenhans I, Stahlmann J, Reedlum B (2022) WEIMOS: Creep of rock salt at low deviatoric stresses. In: de Bresser JHP, Drury MR, Fokker PA, Gazzani M, Hangx SJT, Niemeijer AR, Spiers CJ (eds) The mechanical behavior of salt. CRC Press

Lüthgens C, Böse M, Preusser F (2011) Age of the Pomeranian ice-marginal position in northeastern Germany determined by Optically Stimulated Luminescence (OSL) dating of glaciofluvial sediments. Boreas 40:598–615. https://doi.org/10.1111/j.1502-3885.2011.00211.x

Mukherjee S, Talbot CJ, Koyi HA (2010) Viscosity estimates of salt in the Hormuz and Namakdan salt diapirs, Persian Gulf. Geol Mag 147:497–507. https://doi.org/10.1017/S001675680999077X

Müller U, Obst K (2008) Junge halokinetische Bewegungen im Bereich der Salzkissen Schlieven und Marnitz in Südwest-Mecklenburg. Brandenburg Geowiss Beitr 15:147–154

Nikolinakou MA, Luo G, Hudec MR, Flemings PB (2012) Geomechanical modeling of stresses adjacent to salt bodies: Part 2 - Poroelastoplasticity and coupled overpressures. AAPG Bull 96:65–85. https://doi.org/10.1306/04111110143

Nikolinakou MA, Flemings PB, Hudec MR (2014) Modeling stress evolution around a rising salt diapir. Mar Petrol Geol 51:230–238. https://doi.org/10.1016/j.marpetgeo.2013.11.021

Rowan MG, Urai JL, Fiduk JC, Kukla PA (2019) Deformation of intra-salt competent layers in different modes of salt tectonics. Solid Earth 10:987–1013. https://doi.org/10.5194/se-10-987-2019

Schléder Z, Urai JL (2005) Microstructural evolution of deformation-modified primary halite from the Middle Triassic Röt Formation at Hengelo, The Netherlands. Int J Earth Sci 94:941–955. https://doi.org/10.1007/s00531-005-0503-2

Schléder Z, Urai JL (2007) Deformation and recrystallization mechanisms in mylonitic shear zones in naturally deformed extrusive Eocene-Oligocene rocksalt from Eyvanekey plateau and Garmsar hills (central Iran). J Struct Geol 29:241–255. https://doi.org/10.1016/j.jsg.2006.08.014

Sirocko F, Szeder T, Seelos C, Lehné R, Rein B, Schneider WM, Dimke M (2002) Young tectonic and halokinetic movements in the North-German-Basin: its effect on formation of modern rivers and surface morphology. Netherl J Geosci 81:431–441. https://doi.org/10.1017/S0016774600022708

Sirocko F, Reicherter K, Lehné R, Hübscher C, Winsemann J, Stackebrandt W (2008) Glaciation, salt and the present landscape. In: Littke R, Bayer U, Gajewski D, Nelskamp S (eds) Dynamics of Complex Intracontinental Basins – the Central European Basin System. Springer, Berlin, pp 233–245

Spiers CJ, Carter NL (1998) Microphysics of rock salt flow in nature. In: Aubertin M, Hardy HR (eds) Fourth Conference on the Mechanical Behavior of Salt. USA

Spiers CJ, Schutjens PMTM, Brzesowsky RH, Peach CJ, Liezenberg JL, Zwart HJ (1990) Experimental determination of constitutive parameters governing creep of rocksalt by pressure solution. Geol Soc Lond Spec Pub 54:215–227. https://doi.org/10.1144/GSL.SP.1990.054.01.21

Stackebrandt W (2005) Neotektonische Aktivitätsgebiete in Brandenburg (Norddeutschland). Brandenburg Geowiss Beitr 12:165–172

Stackebrandt W (2016) Nachweis junger geologischer Aktivitäten des Diapirs von Sperenberg (Brandenburg) mittels Laserscanaufnahmen. Brandenburg Geowiss Beitr 23:77–83

Steffen H, Wu P (2011) Glacial isostatic adjustment in Fennoscandia – a review of data and modeling. J Geodyn 52:169–204. https://doi.org/10.1016/j.jog.2011.03.002

Stewart IS, Sauber J, Rose J (2000) Glacio-seismotectonics: ice sheets, crustal deformation and seismicity. Quat Sci Rev 19:1367–1389. https://doi.org/10.1016/S0277-3791(00)00094-9

Talbot CJ (1999) Ice ages and nuclear waste isolation. Eng Geol 52:177–192. https://doi.org/10.1016/S0013-7952(99)00005-8

Ter Heege JD, De Bresser JHP, Spiers CJ (2005) Dynamic recrystallization of wet synthetic polycrystalline halite: dependence of grain size distribution on flow stress, temperature and strain. Tectonophys 396:35–57. https://doi.org/10.1016/j.tecto.2004.10.002

Turcotte DL, Schubert G (2002) Geodynamics. Cambridge University Press, Cambridge

Urai JL, Spiers CJ, Zwart HJ, Lister GS (1986) Weakening of rock salt by water during long-term creep. Nature 324:554–557

Urai JL, Spiers CJ (2007) The effect of grain boundary water on deformation mechanisms and rheology of rock salt during long-term deformation. In: Wallner M, Lux K, Minkley W, Hardy H (eds) Proceedings of Sixth Conference on the Mechanical Behavior of Salt.

Urai JL, Schléder Z, Spiers CJ, Kukla PA (2008) Flow and transport properties of salt rocks. In: Littke R, Bayer U, Gajewski D, Nelskamp S (eds) Dynamics of Complex Intracontinental Basins – the Central European Basin System. Springer, Berlin, pp 277–290

Van Keken PE, Spiers CJ, van den Berg AP, Muyzert EJ (1993) The effective viscosity of rock salt: implementation of steady-state creep laws in numerical models of salt diapirism. Tectonophys 225:457–476. https://doi.org/10.1016/0040-1951(93)90310-G

Vendeville BC (2005) Salt tectonics driven by sediment progradation: Part I - Mechanics and kinematics. AAPG Bull 89:1071–1079. https://doi.org/10.1306/03310503063

Walcott RI (1970) Isostatic response to loading of the crust in Canada. Can J Earth Sci 7:716–727

Waldron JW, Rygel MC (2005) Role of evaporite withdrawal in the preservation of a unique coal-bearing succession: *Pennsylvanian joggins* formation, nova scotia. Geology 33:337–340. https://doi.org/10.1130/G21302.1

Warren JK (2006) Evaporites: sediments, resources and hydrocarbons. Springer, Berlin

Warsitzka M, Jähne-Klingberg F, Kley J, Kukowski N (2019) The timing of salt structure growth in the Southern Permian basin (Central Europe) and implications for basin dynamics. Basin Res 31:337–360. https://doi.org/10.1111/bre.12323

Weijermars R, Jackson MPA, Vendeville BC (1993) Rheological and tectonic modeling of salt provinces. Tectonophys 217:143–174. https://doi.org/10.1016/0040-1951(93)90208-2

Winsemann J, Koopmann H, Tanner DC, Lutz R, Lang J, Brandes C, Gaedicke C (2020) Seismic interpretation and structural restoration of the Heligoland glaciotectonic thrust-fault complex: Implications for multiple deformation during (pre-) Elsterian to Warthian ice advances into the southern North Sea Basin. Quat Sci Rev 227:106068

Wu S, Bally AW, Cramez C (1990) Allochthonous salt, structure and stratigraphy of the north-eastern Gulf of Mexico. Part II: Structure Mar Petrol Geol 7:334–370. https://doi.org/10.1016/0264-8172(90)90014-8

Zienkiewicz OC, Taylor RL (2005) The finite element method for solid and structural mechanics. Elsevier, Amsterdam

Zill F, Wang W, Nagel T (2022) Influence of THM process coupling and constitutive models on the simulated evolution of deep salt formations during glaciation. In: de Bresser JHP, Drury MR, Fokker PA, Gazzani M, Hangx SJT, Niemeijer AR, Spiers CJ (eds) The mechanical behavior of salt. CRC Press, London